Pergamon

Geochimica et Cosmochimica Acta, Vol. 63, No. 23/24, pp. 4119–4138, 1999

0016-7037/99 $20.00 + .00

PII S0016-7037(99)00313-0

Porosity of the melting zone and variations in the solid mantle upwelling rate beneath Hawaii: Inferences from ^{238}U-^{230}Th-^{226}Ra and ^{235}U-^{231}Pa disequilibria

K. W. W. Sims,[1,2,3,*] D. J. DePaolo,[1] M. T. Murrell,[2] W. S. Baldridge,[2] S. Goldstein,[2] D. Clague,[4] and M. Jull[3]

[1]Berkeley Center for Isotope Geochemistry, Department of Geology & Geophysics, University of California, Berkeley, Berkeley, CA 94720, USA
[2]Los Alamos National Laboratory, Los Alamos, NM 87545, USA
[3]Department of Geology & Geophysics, Woods Hole Oceanographic Institution, Woods Hole, MA 02543, USA
[4]Monterey Bay Aquarium Research Institute, 7700 Sandholdt Rd., Moss Landing, CA 95039, USA

(*Received June* 26, 1998; *accepted in revised form June* 6, 1999)

Abstract—Measurements of ^{238}U-^{230}Th-^{226}Ra and ^{235}U-^{231}Pa disequilibria in a suite of tholeiitic-to-basanitic lavas provide estimates of porosity, solid mantle upwelling rate and melt transport times beneath Hawaii. The observation that (^{230}Th/^{238}U) > 1 indicates that garnet is required as a residual phase in the magma sources for all of the lavas. Both chromatographic porous flow and dynamic melting of a garnet peridotite source can adequately explain the combined U-Th-Ra and U-Pa data for these Hawaiian basalts. For chromatographic porous flow, the calculated maximum porosity in the melting zone ranges from 0.3–3% for tholeiites and 0.1–1% for alkali basalts and basanites, and solid mantle upwelling rates range from 40 to 100 cm yr^{-1} for tholeiites and from 1 to 3 cm yr^{-1} for basanites. For dynamic melting, the escape or threshold porosity is 0.5–2% for tholeiites and 0.1–0.8% for alkali basalts and basanites, and solid mantle upwelling rates range from 10 to 30 cm yr^{-1} for tholeiites and from 0.1 to 1 cm yr^{-1} for basanites. Assuming a constant melt productivity, calculated total melt fractions range from 15% for the tholeiitic basalts to 3% for alkali basalts and basanites.

1. INTRODUCTION

The formation and transport of basaltic magma in the mantle by adiabatic decompression can be characterized in terms of the velocity of the upwelling (solid) mantle, the rate of melting, the melt velocity and the dispersity associated with melt migration, and the delay time, or storage time, of magma before eruption (e.g., Stolper et al., 1981; Turcotte, 1982; McKenzie, 1984, 1985; Richter and McKenzie, 1984; Ribe, 1985, 1987; DePaolo, 1996). Two of these parameters, the velocity of upwelling mantle and the corresponding melting rate, can be estimated from models coupled with thermodynamic data and geophysical observations (e.g., McKenzie and Bickle, 1988; Watson and McKenzie, 1991; Forsyth, 1992; Asimov et al., 1997). The melt velocity, dispersivity of the melt zone, and the storage times, on the other hand, are difficult to estimate from first principles and require measurement. These parameters can be measured indirectly by geochemical methods. In particular, the departures from radioactive equilibrium observed for several nuclides in the U-decay series give information on the rate of melting, the melt migration velocity, and the extent of melting (McKenzie, 1985; Williams and Gill, 1989; Spiegelman and Elliot, 1993; Elliot, 1997).

The daughter isotopes ^{230}Th and ^{226}Ra of the ^{238}U-decay series, and ^{231}Pa of the ^{235}U-decay series have half-lives (75.4 Kyr, 1.6 Kyr, and 32.8 Kyr respectively) which bracket the time-scales over which melting and melt extraction are thought to occur. Because the half-lives are appropriate, and there are large differences in the solid/liquid partition coefficients for U versus Th, Th versus Ra, and U versus Pa, measurements of ^{230}Th/^{238}U, ^{226}Ra/^{230}Th and ^{231}Pa/^{235}U ratios in young basaltic lavas provide information on the time scales of melt generation. Models that relate the isotopic effects of U-series-decay-rate disequilibria to the melting process have been described by McKenzie (1985), Williams and Gill (1989), Spiegelman and Elliot (1993), Qin (1993), Iwamori (1994), and Richardson and McKenzie (1994). The lack of precision afforded by the traditional counting methods used for measurements of (^{230}Th/^{238}U) and (^{226}Ra/^{230}Th) disequilibria in young basaltic samples have thus far limited the application of the models. Furthermore, most studies have focused on mid-ocean ridge basalt (MORB) (Condomines et al., 1981; Newman et al., 1983; Rubin and Macdougall, 1988; Reinitz and Turekian, 1989; Ben Othman and Allegre, 1990; Goldstein et al., 1989, 1992; Volpe and Goldstein, 1993; Lundstrom et al., 1995; Bourdon et al., 1996) which show a pattern of trace-element fractionation which is more complex than that observed in ocean island basalts (OIB) such as Hawaii (Cohen and O'Nions, 1993; Hemond et al., 1994; Chabaux and Allegre, 1994; Sims et al., 1995; Elliot, 1997; Condomines et al., 1981).

We report ^{238}U-^{230}Th-^{226}Ra and ^{235}U-^{231}Pa isotopic measurements on basaltic lavas from Hawaii, using recently developed thermal ionization mass spectrometric (TIMS) techniques (Goldstein et al., 1989; Volpe et al., 1993; Pickett et al., 1994; Chabaux et al., 1994) which afford improved resolution for measuring the small departures from radioactive equilibrium in the U-decay series. In a previous publication, ^{238}U-^{230}Th isotopic data were reported for many of these lava samples (Sims et al., 1995). In this work we add measurements of ^{226}Ra and ^{231}Pa, which greatly enhance the constraints on the melting process because of their shorter half-lives.

* Author to whom correspondence should be addressed (ksims@mail.whoi.edu).

Table 1. Sample ages and location.

Sample	Location/Flow name	Eruption Date/Radiocarbon Age	Ref.
Kilauea			
Kl-01-KWWS-92	Pu'u O'o flow: Kalapana	1990	1
KL-F91-31	collected from Pu'u O'o vent	07/31/91	2
KL-F91-32	collected from Pu'u O'o vent	08/02/91	2
Mauna Loa			
ML-61-KWWS-92	Saddle Road Flow	1935	3
ML-07-KWWS-92	Hwy 190: NE Puuanahula	1861	3
Mauna Kea			
MK-06-KWWS-92	Kalaleha Flow: lower So. flank	5630 ± 200	4
MK-12-KWWS-92	Flow So. of Hookomo: lower So. flank	5320 ± 150	4
Hualalai			
HU-05-KWWS-92	Hue Hue Flow: vent area	1801	5
HU-10-KWWS-92	Unit f6d p24-near summit	1,030 ± 60	5
HU-13-KWWS-92	Unit f5d q1-near summit	2,290 ± 70	5
HU-18-KWWS-92	Waha Pele	710 ± 150	5
HU-24-KWWS-92	Kaupulehu Flow	1801	5
Haleakala			
HK-02-KWWS-92	Kalua O Lapa Flow	1792	6
HK-04-KWWS-92	Kamahina Flow	200–900	6
HK-06-KWWS-92	Luepalani Flow	200–1000	6
HK-10-KWWS-92	Luepalani Flow	200–1000	6
HK-11-KWWS-92	Pimoe Flow	200–1000	6

Sample ages from: 1 Hon et al., 1994. 2 collected by F. Goff. 3 Lockwood et al., 1988. 4 Porter, 1979. 5 Moore and Clague, 1981. 6 Reber, 1959; Oostdam, 1965; Crandell, 1983. For locations and ages of Loihi samples see Moore et al., 1982.

The lava samples used here encompass a range in chemical composition from tholeiite to basanite. The samples are all either historical flows or have been dated by radiocarbon, and were collected from the Loihi, Mauna Loa, Kilauea, Mauna Kea, Hualalai and Haleakala volcanoes. The sample suite represents most of the range of lava chemistry exhibited by Hawaiian lavas, and this range is believed to stem from variations in the melting parameters as the volcanoes, carried by the moving Pacific plate, traverse the Hawaiian mantle plume. Our sample suite, including most of the volcanoes that extend from the leading edge to the trailing edge of the plume, and encompassing the full range of lava compositions, provides a snapshot (albeit crude) of the melting process extending from the core of the plume to its fringes.

In our previous study, which involved only measurements of ^{230}Th-^{238}U decay disequilibria, we emphasized the constraints that were placed on the extent of melting, using batch melting models. The ^{230}Th-^{238}U decay disequilibria are mainly sensitive to melt fraction because of the long half-life of ^{230}Th. However, interpretation of ^{226}Ra data, because of its much shorter half-life, requires models that treat explicitly the time-scales of melt generation and melt extraction (e.g., McKenzie, 1985; Spiegelman and Elliot, 1993). From the combined ^{230}Th/^{238}U, ^{226}Ra/^{230}Th and ^{231}Pa/^{235}U data and using both a chromatographic porous flow melting model and a dynamic (or near-fractional) melting model we are able to obtain estimates of porosity and solid mantle upwelling velocity. These parameters are then used to constrain melting conditions in the Hawaiian plume. The incorporation of melt migration time-scales and chromatographic effects changes our estimates of melt fraction relative to those previously inferred from batch melting models (Sims et al., 1995). The ^{226}Ra/^{230}Th measurements also limit magma chamber residence times.

2. SAMPLES

Sample locations and ages are given in Table 1. For the isotopes of the U-decay series, knowledge of the eruption age of the samples is critical to the interpretation of the data. The Kilauea and Mauna Loa samples are from historical flows. The samples from Hualalai, Mauna Kea and Haleakala were collected from either historic or young, radiocarbon-dated flows. The Loihi samples are dive or dredge samples collected from submarine surface flows; their ages are estimated to be less than 10,000 years based on measured thicknesses of palagonite rinds.

Major- and trace-element concentrations and Nd and Sr isotopes are reported in Appendix 2. The compositions extend from olivine-tholeiite to silica-undersaturated basanite. With the exception of the Mauna Kea samples which are evolved hawaiite, the samples represented in this study are relatively undifferentiated, as indicated by their high MgO (>7%), Ni and Cr contents. All of the samples used in this study were fresh hand-picked interior pieces and have $K_2O/P_2O_5 > 1$ and (^{234}U/^{238}U) activity ratios = 1, indicating minimal post-eruptive alteration. (Activity ratios are hereafter noted with parentheses.) K_2O/P_2O_5 ratios and (^{234}U/^{238}U) of less than one can reflect the effects of weathering because of preferential loss of K_2O and ^{234}U during alteration. Because of the long half-life of ^{234}U, for young subareial samples such as these, (^{234}U/^{238}U) of one are a necessary, but not sufficient condition for ruling out secondary alteration.

3. U-SERIES DISEQUILIBRIUM MEASUREMENTS IN HAWAIIAN BASALTS

U, Th, Pa and Ra concentrations and (^{234}U/^{238}U), (^{230}Th/^{232}Th), (^{230}Th/^{238}U), (^{226}Ra/^{230}Th) (^{231}Pa/^{235}U) for the Hawaiian samples are reported in Table 2. These measurements

Table 2. (^{230}Th/^{232}Th), (^{230}Th/^{238}U), (^{226}Ra/^{230}Th), (^{231}Pa/^{235}U), ^{234}U/^{238}U, and U, Th, Pa and Ra concentrations measured by TIMS.

Sample	[Th][1] μg/g	[U][1] μg/g	[Ra][1] fg/g	[Pa][1] fg/g	(^{230}Th/^{232}Th)[2]	(^{230}Th/^{238}U)[3]	(^{226}Ra/^{230}Th)[4] measured	(^{226}Ra/^{230}Th)[5] age corr.	(^{231}Pa/^{235}U)[6]	^{234}U/^{238}U[7] ×10^{-6}
Loihi										
KK-19-1 (WR)	0.775	0.236	**	**	0.964	1.044	**	**	**	**
KK-19-1 (Gl) (1)	0.774	0.236	**	**	0.967	1.045	**	**	**	55.243
KK-19-1 (Gl) (2)[8]	**	0.239	**	89.14	**	**	**	**	1.147	**
KK-27e-14 (1)	0.829	0.243	**	**	0.958	1.077	**	**	**	54.875
KK-27e-14 (2)	**	0.240	**	94.43	**	**	**	**	1.233	**
Kilauea										
Kl-01-KWWS-92	0.867	0.286	**	**	1.041	1.040	**	**	**	54.591
KL-F91-31[9] (1)	0.861	0.290	110.98	**	1.049	1.027	1.104	1.104	**	54.584
KL-F91-31 (2)	**	0.284	**	100.62	**	**	**	**	1.097	**
KL-F91-32[9] (1)	0.826	0.281	**	**	1.048	1.016	**	**	**	54.685
KL-F91-32 (2)	**	0.281	**	100.58	**	**	**	**	1.100	**
Mauna Loa										
ML-61-KWWS-92[10] (1)	0.552	0.185	74.31	**	1.051	1.034	1.151	1.155	**	54.399
ML-61-KWWS-92 (2)	**	0.182	**	67.04	**	**	**	**	1.135	**
ML-07-KWWS-92 (1)	0.568	0.193	**	**	1.076	1.044	**	**	**	54.588
ML-07-KWWS-92 (2)	**	0.195	**	71.97	**	**	**	**	1.138	**
Mauna Kea										
MK-06-KWWS-92	3.93	1.247	**	**	1.102	1.145	**	**	**	54.798
MK-12-KWWS-92	4.299	1.254	**	**	1.097	1.240	**	**	**	54.820
Hualalai										
HU-05-KWWS-92	1.611	0.456	239.79	**	1.002	1.167	1.335	1.364	**	54.890
HU-10-KWWS-92 (1)	1.433	0.409	187.72	**	1.026	1.185	1.147	1.23 ± 0.01	**	54.990
HU-10-KWWS-92 (2)	**	0.410	**	197.31	**	**	**	**	1.481	**
HU-13-KWWS-92	1.53	0.446	189.19	**	1.009	1.141	1.101	1.27 ± 0.01	**	**
HU-18-KWWS-92 (1)	1.56	0.440	198.17	**	1.009	1.179	1.131	1.18 ± 0.02	**	54.972
HU-18-KWWS-92 (2)	**	0.441	**	215.00	**	**	**	**	1.498	**
HU-24-KWWS-92 (1)	1.654	0.480	242.07	**	1.024	1.163	1.284	1.309	**	54.752
HU-24-KWWS-92 (2)	**	0.485	**	232.97	**	**	**	**	1.477	**
Haleakala										
HK-02-KWWS-92	3.472	0.981	524.06	**	1.099	1.282	1.234	1.256	**	**
HK-04-KWWS-92 (1)	2.369	0.660	359.44	**	1.105	1.308	1.234	1.29 ± 0.05	**	55.036
HK-04-KWWS-92 (2)	**	0.661	**	383.04	**	**	**	**	1.783	**
HK-06-KWWS-92 (1)	3.423	1.003	517.35	**	1.105	1.243	1.229	1.30 ± 0.06	**	54.836
HK-06-KWWS-92 (2)	**	0.979	**	526.10	**	**	**	**	1.673	**
HK-10-KWWS-92 (1)	3.350	0.993	498.45	**	1.103	1.226	1.213	1.28 ± 0.06	**	54.873
HK-10-KWWS-92 (2)	**	0.997	**	537.99	**	**	**	**	1.658	**
HK-11-KWWS-92 (1)	3.761	1.042	553.75	**	1.102	1.311	1.201	1.26 ± 0.05	**	**
HK-11-KWWS-92 (2)	**	1.041	**	590.44	**	**	**	**	1.734	**
Table Mountain Latite										
TML-1	29.56	10.54	3569	3,428	1.084	1.002	1.003	**	1.000[11]	54.810
TML-2	29.91	10.56	3564	3,424	1.074	1.003	0.997	**	0.997	54.707

Notes:

[1] [U], [Th], [Pa], and [Ra] measured by ID-TIMS; measurement errors in [U], [Th] ≤ 0.5%, [Ra], [Pa] ≤ 0.8%.

[2] ( ) denotes activity; $\lambda_{230} = 9.195 \times 10^{-6}$ yr^{-1}, $\lambda_{232} = 4.948 \times 10^{-11}$ yr^{-1}; measured by HAS-TIMS; errors (2σ) range from: 0.5%–0.8% and do not include uncertainties in λ_{230} (0.4%) or λ_{232} (0.5%).

[3] $\lambda_{238} = 1.551 \times 10^{-10}$ yr^{-1}; errors (2σ) range from 0.4%–0.5% and do not include uncertainties in λ_{238} (0.07%) or λ_{230}.

[4] $\lambda_{226} = 4.331 \times 10^{-4}$ yr^{-1}, errors (2σ) range from 0.6%–0.9% and do not include uncertainties in λ_{226} (0.4%) or λ_{230}.

[5] For non-historic samples, error primarily represents uncertainty in ^{14}C ages (see Table 1).

[6] $\lambda_{231} = 2.115 \times 10^{-5}$ yr^{-1}, errors (2σ) range from 0.6%–0.9% and do not include uncertainties in λ_{231} (0.4%) or λ_{235} (0.07%).

[7] $\lambda_{234} = 2.823 \times 10^{-6}$ yr^{-1}, errors (2σ) < 1.0%; for these samples (^{234}U/^{238}U) = 1 within error, using an equilibrium ^{234}U/^{238}U of 54.95 ppm.

[8] Analyses for ^{235}U-^{231}Pa are from same samples but separate powder splits.

[9] Results of independent analyses of 1991 flows from Puu O'o agree within measurement error (Petruzska et al. unpublished data)

[10] Results of an independent analysis on same flow by Cohen et al. (1993) agree within measurement error.

[11] TML-1 used to calibrate ^{233}Pa spike, but measured as an unknown for U-Th-Ra disequilibria; TML-2 measured as unknown for U-Th-Ra and U-Pa disequilibria.

were made by isotope dilution and mass spectrometric methods. For many of these samples Sm, Nd, Th and U isotopes and concentrations have been previously reported (Sims et al., 1995). The (^{238}U/^{232}Th), (^{230}Th/^{238}U) and (^{226}Ra/^{230}Th) measurements for the tholeiites from Kilauea and Mauna Loa are consistent with other TIMS measurements for these same basalts (Cohen et al., 1993; Petruzska et al, unpublished data).

3.1. ^{238}U-^{230}Th Disequilibria

In all of the Hawaiian samples examined, (^{230}Th/^{238}U) > 1, indicating that Th is enriched relative to U (Fig. 1a). An important first-order observation is that there is a systematic correlation between basalt type and the extent of (^{230}Th/^{238}U) disequilibrium: tholeiites show the least amount of disequilib-

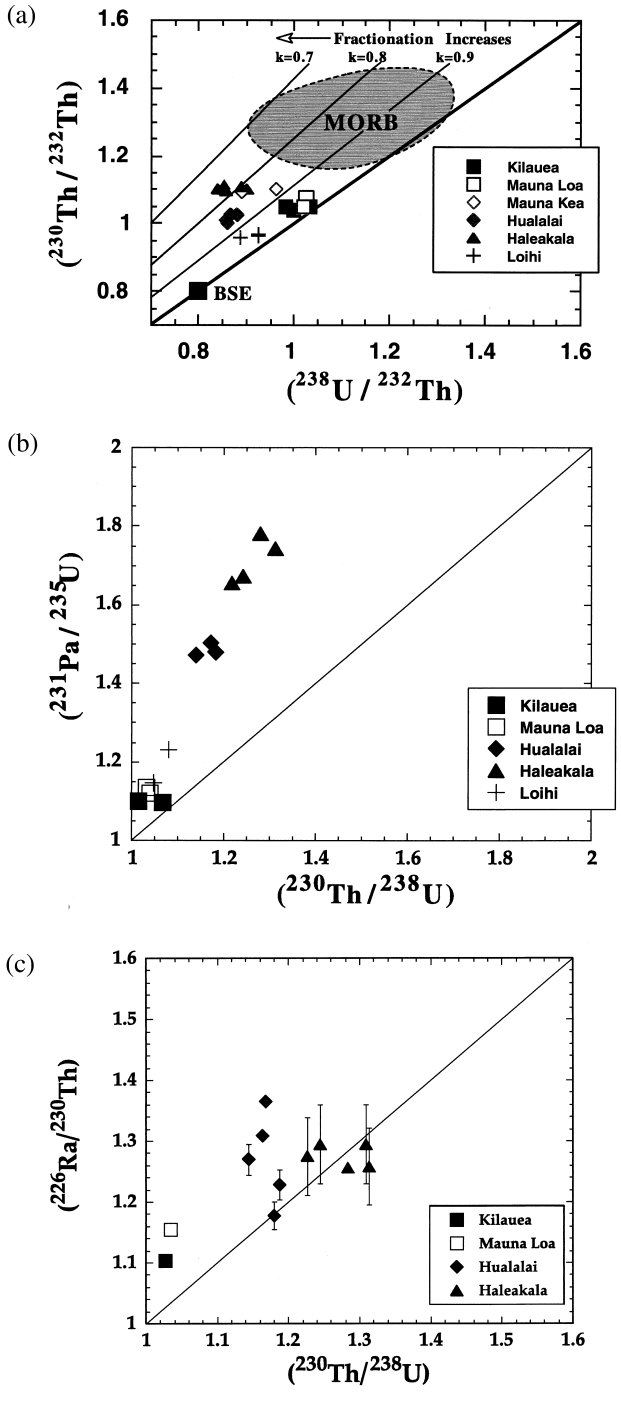

Fig. 1. **a.** (^{230}Th/^{232}Th) vs (^{238}U/^{232}Th); **b.** (^{231}Pa/^{235}U) vs. (^{230}Th/^{238}U); **c.** (^{226}Ra/^{230}Th) vs. (^{230}Th/^{238}U) for the Hawaiian samples. Sizes of data points are larger than the propagated relative measurement errors; for (^{226}Ra/^{230}Th) error bars on non-historic samples represent uncertainties in ^{14}C age (see Table 1).

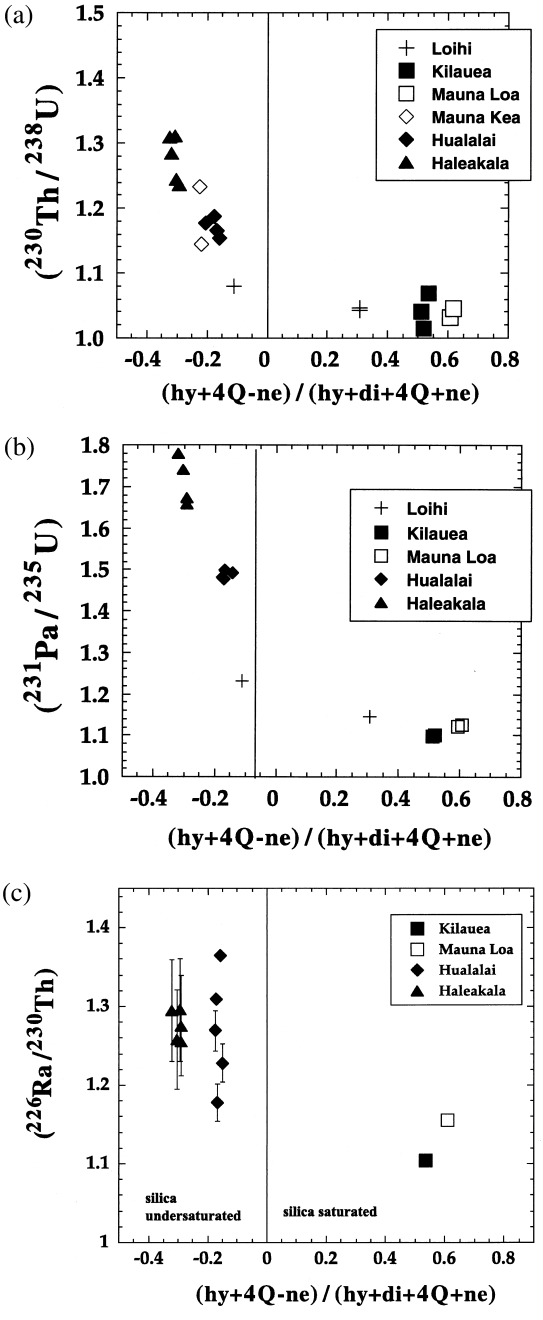

Fig. 2. **a.** (^{230}Th/^{238}U) versus (hy + 4Q − ne)/(hy + di + 4Q + ne) **b.** (^{231}Pa/^{235}U) versus (hy + 4Q − ne)/(hy + di + 4Q + ne); **c.** (^{226}Ra/^{230}Th) versus (hy + 4Q − ne)/(hy + di + 4Q + ne) for the Hawaiian samples.

rium and alkali basalts and basanites show progressively larger amounts. When the compositional range of these samples is quantified in terms of normative hypersthene and nepheline content there is an excellent correlation between (^{230}Th/^{238}U) and silica saturation index (Fig. 2a). Similar correlations are seen with SiO_2, or other major-element parameters such as Mg normalized Na content (Sims et al., 1995). For the Hawaiian data there is also a systematic relation between U/Th fractionation and Sm/Nd fractionation (denoted as $\alpha_{Sm/Nd}$), with Sm/Nd more fractionated than U/Th (Fig. 3a).

3.2. ^{235}U-^{231}Pa Disequilibria

(^{231}Pa/^{235}U) is greater than one in all of the Hawaiian samples, indicating that Pa is enriched in basaltic melts relative

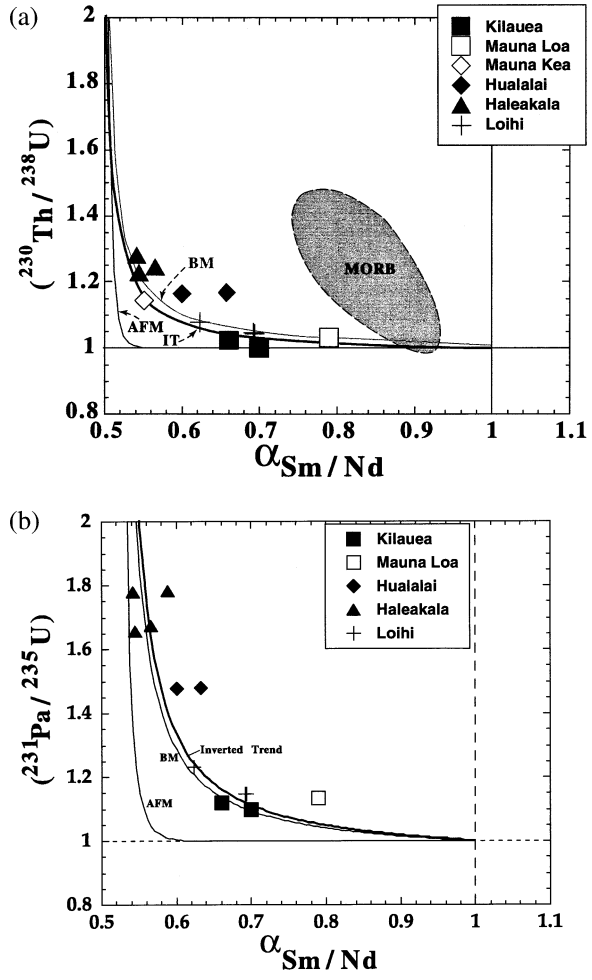

Fig. 3. **a.** (^{230}Th/^{238}U) vs. $\alpha_{Sm/Nd}$ and **b.** (^{231}Pa/^{235}U) vs. $\alpha_{Sm/Nd}$ for Hawaiian samples. Where $\alpha_{Sm/Nd}$ is a measure of the Sm/Nd fractionation during basalt petrogenesis and is the Sm/Nd concentration ratio measured in the lava normalized to a model Sm/Nd source ratio inferred from the measured ^{143}Nd/^{144}Nd of the lava (for details see DePaolo, 1988; Salters and Hart, 1989; and Sims et al., 1995). Shown are batch melting (BM) and accumulated fractional melting (AFM) trends for a garnet lherzolite source (8% cpx; 12% garnet) using measured D_{Sm} and D_{Nd} values from McKay, 1985 and measured D_U and D_{Th} values from La Tourrette et al., 1993; Lundstrom et al., 1994, and an inferred D_{Pa} value (Table 3). Also shown is the best-fit trend used to invert the data to find self-consistent bulk D_U/D_{Th}-D_{Sm}/D_{Nd} and D_U/D_{Pa}-D_{Sm}/D_{Nd} values. This inversion assumes batch melting of garnet lherzolite source and uses D_{Sm} and D_{Nd} values from McKay, 1985 (see Sims et al., 1985). The sizes of the data points are larger than the propagated relative measurement errors (2σ). Note: for MORB (^{231}Pa/^{235}U) > 2.0.

to U. There is a systematic correlation between (^{231}Pa/^{235}U) and (^{230}Th/^{238}U) (Fig. 1b); the relative values of these disequilibrium ratios gives an order of incompatibility of $D_{Pa} < D_{Th} < D_U$. Like (^{230}Th/^{238}U), there is also a systematic correlation between basalt type and (^{231}Pa/^{235}U) disequilibrium: tholeiites show the least amount of disequilibrium and alkali basalts and basanites show progressively larger amounts (Fig. 2b). When compared with Sm/Nd fractionation, U/Pa is less fractionated than Sm/Nd in the tholeiitic samples from Kilauea, Mauna Loa and Loihi; but in the alkali basalts and basanites, U/Pa and Sm/Nd show similar amounts of fractionation (Fig. 3b).

3.3. ^{230}Th-^{226}Ra Disequilibria

In all of the Hawaiian samples examined, (^{226}Ra/^{230}Th) is greater than one, indicating that Ra is enriched relative to Th. When (^{226}Ra/^{230}Th) is compared with (^{230}Th/^{238}U) (Fig. 1c) and (^{231}Pa/^{235}U), the relative value of the disequilibrium activity ratios gives an order of incompatibility of $D_{Pa} \approx D_{Ra} < D_{Th} < D_U$. There is a bi-modal relationship between (^{226}Ra/^{230}Th) and the major-element chemistry of these Hawaiian samples: tholeiites show the smallest Ra/Th fractionation while alkali basalts and basanites show higher but similar degrees of Ra/Th fractionation (Fig. 2c). This relationship is markedly different from the systematic relationships observed between (^{230}Th/^{238}U) and (^{231}Pa/^{235}U).

4. COMPARISON OF DATA WITH MELTING MODELS

The activity ratios (^{230}Th/^{238}U), (^{231}Pa/^{235}U), and to a lesser extent (^{226}Ra/^{230}Th), vary systematically as a function of melt composition, and extent of melting as inferred from trace-element compositions. This observation argues that the isotopic variations are a result of melting processes and not secondary alteration (e.g., Hemmond et al., 1994). We argued previously that the observed U/Th fractionation can be accounted for by variations in melt fraction ranging from 6.5% for tholeiites to 0.25% for basanites (Sims et al., 1995). The melt fraction estimates were based on batch melting calculations. The (^{231}Pa/^{235}U) data presented here can also be modeled with the batch melting model. However, the large departures of ^{226}Ra/^{230}Th from equilibrium cannot be explained by batch melting. Because of the short half-life of ^{226}Ra, interpretation of the Hawaiian (^{226}Ra/^{230}Th) disequilibrium data requires models that treat explicitly the time-scale of melt generation and melt extraction (McKenzie, 1985; Williams and Gill, 1989; Spiegelman and Elliot, 1993; Iwamori, 1993; Qin, 1993). As shown below, both chromatographic porous flow and dynamic melting models can adequately explain the combined U-Th-Ra and U-Pa data. The dynamic models also result in somewhat larger inferred melt fractions.

4.1. Chromatographic Porous Flow

The steady state chromatographic porous flow melting model of Spiegelman and Elliot (1993) accounts for the duration of melt generation (i.e., the time it takes the upwelling mantle to traverse the melt column), the relative velocity of the upward-percolating melt and the residual solid, and the effects of continuous melt-solid interaction during melt transport. The model assumes that chemical equilibrium is maintained between migrating liquid and the solid matrix (infinite Damkohler number). Continuous melt-solid interaction produces chromatography; different elements travel through the melt column at different velocities according to their relative melt/solid partition coefficients (i.e., D values). For nonradioactive elements, the steady-state chromatographic porous flow melting model produces trace-element enrichments that are identical to those of equilibrium batch melting (Spiegelman and Elliot, 1993). However, for the U-decay-series isotopes, which have half-

Table 3. Experimentally determined mineral/melt partition coefficients for U, Th, and Ba in Cpx and Gt and bulk partition coefficients calculated for a garnet peridotite source

	Clinopyroxene			Garnet			Garnet Peridotite			
	U	Th	Ba	U	Th	Ba	U	Th	Ra	Pa
Beattie	9.0E-04	1.3E-03	5.0E-04	9.6E-03	1.5E-03	1.0E-05	1.2E-3	2.9E-4	4.0E-5	
Salters and Longi	3.5E-03	3.5E-03	**	4.1E-02	1.9E-02	**	5.3E-3	2.6E-3		**
La Tourette et al.	4.5E-03	1.0E-02	**	1.5E-02	1.7E-03	**	2.2E-3	1.0E-3		**
Lundstrom et al.	1.0E-02	1.5E-02	**	**	**	**	2.6E-3	1.4E-3	(1.0E-5)	(1.3E-04)
Inverted							1.4E-3	6E-4		
Inverted							2.2E-3			1E-4

Experimentally determined mineral/melt partition coefficients for U, Th, and Ba in Cpx and Gt from Beattie, 1993a, b; La Tourette et al., 1992, 1993; Lundstrom et al., 1994; Salters and Longhi, 1999. Bulk partition coefficients for garnet peridotite source calculated using Ol = 59%, Opx = 21%, Cpx = 8%, Gt = 12%. Lundstrom et al. (1994) bulk D values use D_U and D_{Th} for garnet from La Tourrette et al. (1993) and assume that $D_{Pa} = D_U^{5+}$ and D_{Ra} = 1.0E-5. Beattie bulk D_{Ra} value assumes that $D_{Ra} \approx D_{Ba}$. The inverted D_U-D_{Th} and D_U-D_{Pa} values are from correlations of (^{230}Th/^{238}U) and (^{231}Pa/^{235}U) with Sm/Nd fractionation (Figure 3) (see Sims et al., 1995 for details) and are in the range of bulk D values calculated from experimental measurements. This inversion is based upon the equations for batch melting and does not account for the contribution of ingrown ^{230}Th and ^{231}Pa in the measured (^{230}Th/^{238}U) and (^{231}Pa/^{235}U) disequilibria; therefore these estimates of the bulk D_U, D_{Th} and D_{Pa} maximize U/Th and U/Pa fractionation.

lives that are comparable to the melt migration time scales, the chromatographic effect has a significant influence on the resulting concentrations and activity ratios. If the daughter isotope is more incompatible than the parent isotope, which is true for all of the systems considered here, more daughter material is produced in the melt column than was brought in at the bottom and this produces large excesses in daughter isotopes in the resultant basaltic liquids. The extent of this daughter nuclide enhancement depends on the half life of the daughter nuclide, and consequently it is very large for ^{226}Ra, and much smaller for ^{230}Th and ^{231}Pa.

We compare our data to U-series activity ratios calculated from a 1-D numerical model of chromatographic porous flow similar to that of Spiegelman and Elliot (1993) which takes into account a depth dependent porosity. (In Appendix I we contrast analytical solutions which assume a constant porosity to this numerical solution.) The trace element partition coefficients used for the modeling are given in Table 3 and are calculated assuming a garnet peridotite source. The numerical results show that (^{226}Ra/^{230}Th) disequilibrium is controlled mostly by the porosity of the melt region (which controls the velocity of the melt relative to the solid), whereas (^{230}Th/^{238}U) disequilibrium depends mainly on the upwelling rate, which is directly related to the melting rate (Figs. 4 and 5). The overall model has six variable parameters, as outlined in the Appendix: The solid velocity (W_S), the liquid velocity (w), the porosity (ϕ), the height of the melting column (Δz), the melt fraction (F_{max}) and the melting rate (Γ_O). We estimate Δz from the modeling of Watson and McKenzie (1991). Their model indicates that the height of the melting column in the core of the Hawaiian plume is of order 50 km. At distances of 50 km or more from the plume axis, the melt column is estimated to be ~10 km long. Thus we use Δz = 50 km for the tholeiites, and Δz = 10 km for the alkali basalts and basanites. We set the melt productivity $dF/dz = 0.003\ km^{-3}$ (McKenzie and Bickle, 1988). Recent estimates of dF/dz by Asimow et al. (1997) are similar to those deduced by McKenzie and Bickle (1988) in the depth range of interest for Hawaiian magma generation.

Using the average (^{230}Th/^{238}U) and (^{226}Ra/^{230}Th) disequilibria measured for the main-stage tholeiitic basalts, the model calculations (e.g., see Figure 4) indicate that the average porosity of the melting zone is somewhere between 0.3 to 3% and the upwelling rate between 40 to 100 cm yr^{-1}, depending on the partition coefficients used (Table 4). For the alkali basalts from Hualalai, using a melt zone height of 10 km, the calculated porosity ranges from 0.1 to 1% and the upwelling rate ranges from 2 to 5 cm yr^{-1} (Table 4). For the basanites from Haleakala the calculated porosity also ranges between 0.1 to 1%, and the upwelling rate ranges from 1 to 3 cm yr^{-1}.

As a result of the additional ^{230}Th that is produced during melting, the chromatographic porous flow model of Spiegelman and Elliot (1993) estimates total melt fractions (F_{max}) which are considerably higher than those which we previously predicted from simple batch melting (Sims et al., 1995). Using the melt productivity we assume above (dF/dz = 0.003/km) (e.g., McKenzie and Bickle 1988; Asimov et al. 1997) and a melt zone thickness of 50 km for tholeiitic basalts and 10 km for alkali basalts and basanites, we calculate 15% total melt fractions for the tholeiitic basalts and 3% for the alkali basalts and basanites.

4.2. Dynamic Melting

In the "dynamic melting" model, as formulated by McKenzie (1985), melts produced in the upwelling mantle remain trapped, and in equilibrium with the solid residue until a critical threshold porosity is reached, after which any produced melt in excess of the threshold value escapes instantaneously. Dynamic melting takes into consideration the time-scale of the melting process and consequently, like the Spiegelman and Elliot model, produces enhanced excesses of short-lived daughter nuclides like ^{226}Ra. Dynamic melting differs from chromatographic melting in that melts move instantly to the surface as they form and do not react with the solid on the way. As a result, disequilibria is created only at the bottom of the melt column instead of throughout. Unlike chromatographic porous flow where melt velocities are determined explicitly, with dynamic melting melt velocities are constrained by the shortest half-life of the daughter nuclides not in radioactive equilibrium with its immediate parent (e.g., ^{226}Ra). Above the point where

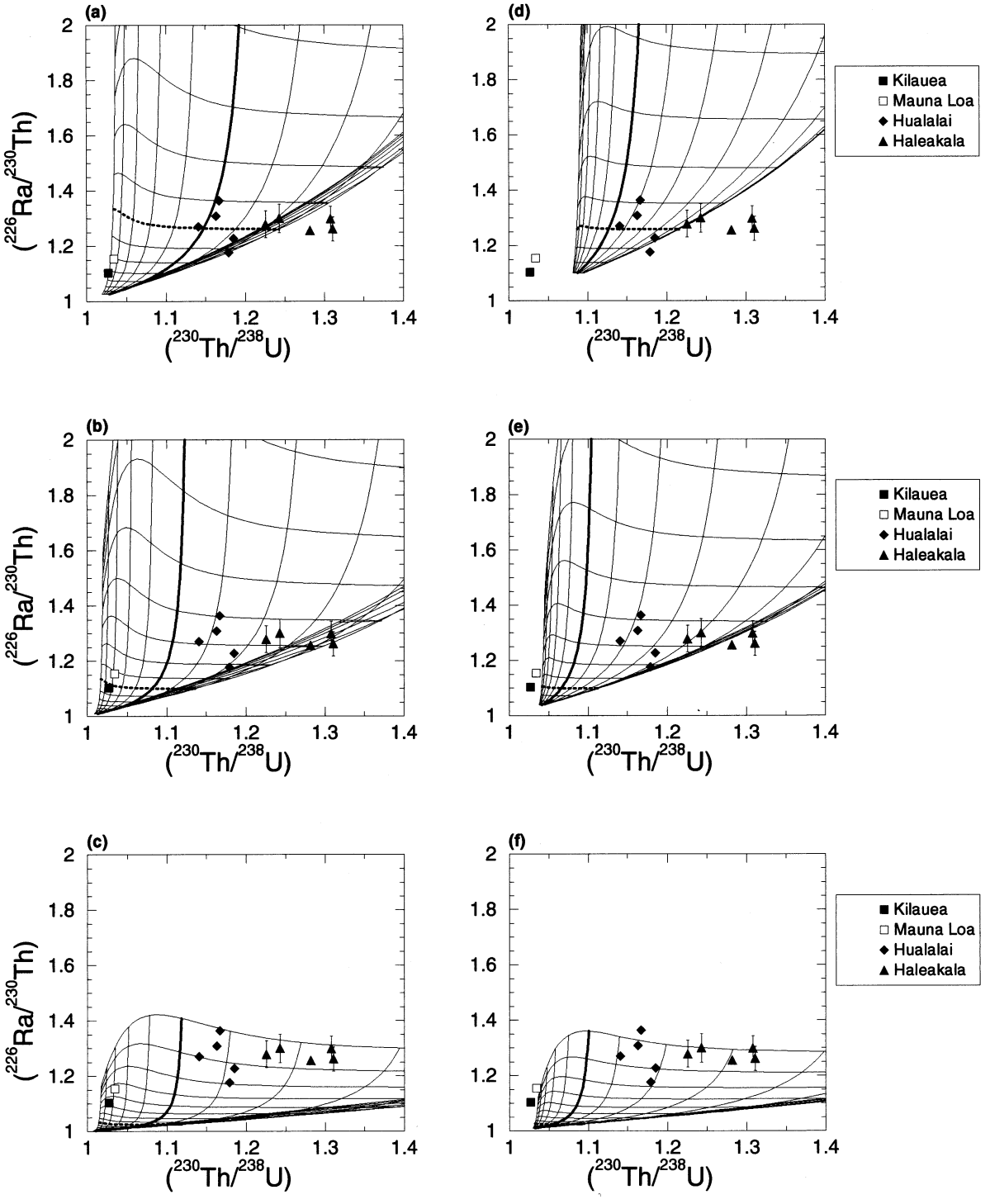

Fig. 4. Comparison of the measured ($^{226}Ra/^{230}Th$) and ($^{230}Th/^{238}U$) for the Hawaiian basalts (symbols) to the calculated values (curves) for chromatographic flow through a 1D melt column. The left column of graphs show the results calculated for a 50 km melt column, using the partition coefficients of (a) Salters and Longi, (b) La Tourette et al, and (c) Beattie et al (Table 3). The right column of graphs show the results calculated for a 10 km melt column, with the partition coefficients corresponding to those shown on the left. The horizontally trending curves show activity ratios for constant maximum porosity (ϕ_{max}) in percent, while the vertically trending contours show the activity ratios for a constant upwelling rate (W_s) in cm/yr. The bold solid contour in each plot shows a reference upwelling rate of 10 cm/yr, while the bold dashed curve shows a reference maximum porosity of about 1%. Spacing between curves is calculated in log units: increments between curves of solid upwelling rate are $10^{0.2}$ cm/yr, and between curves of constant maximum porosity $10^{0.13}$%. The decrease of ($^{230}Th/^{238}U$) at very low upwelling rates is a result of the melting rate approaching the time-scale of the half-life of ^{230}Th. Error bars for ($^{226}Ra/^{230}Th$) reflect the uncertainties in ^{14}C ages (Table 1).

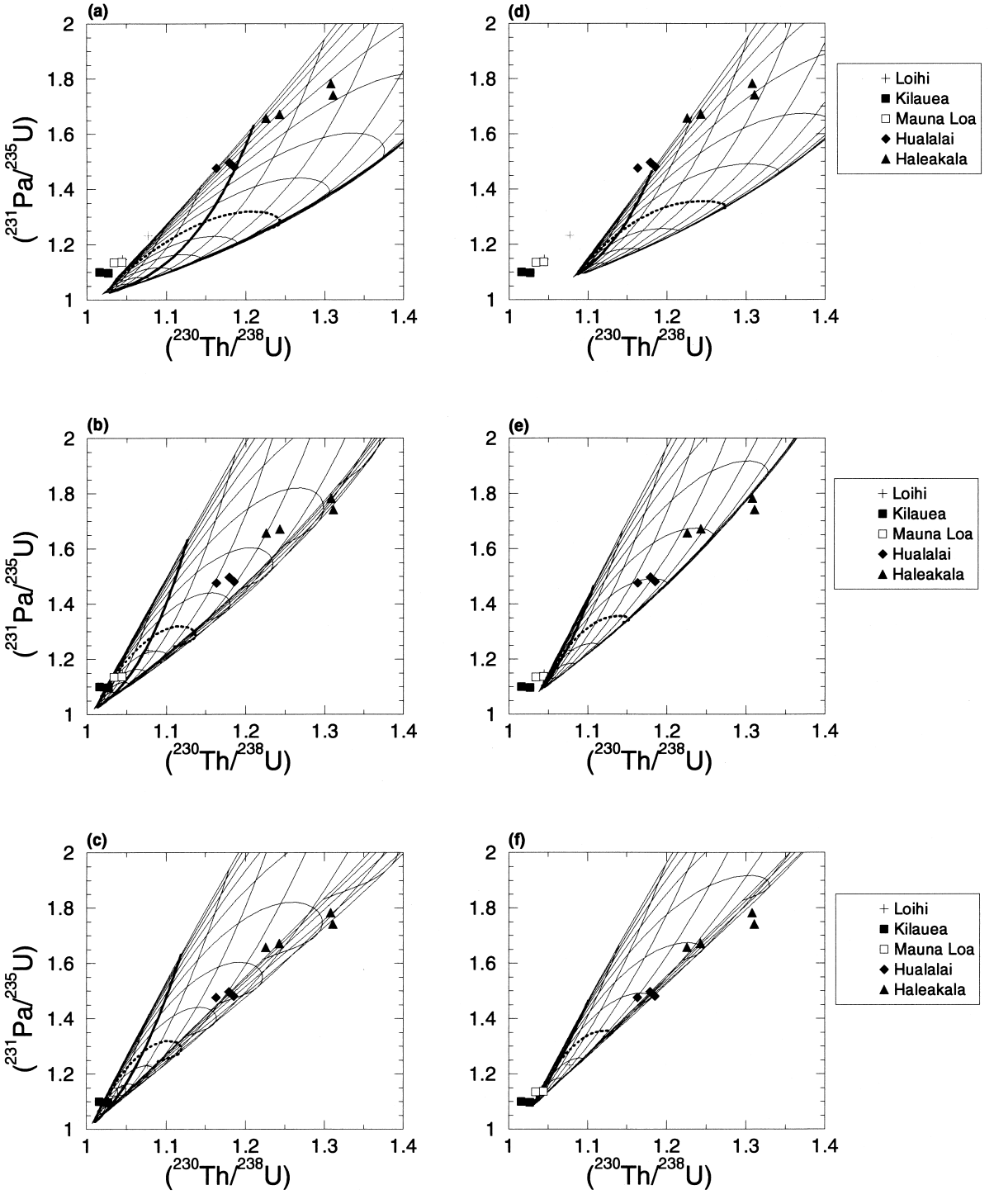

Fig. 5. Comparison of the measured (^{231}Pa/^{238}U) and (^{230}Th/^{238}U) for the Hawaiian basalts (symbols) to the calculated values (curves) for chromatographic flow through a 1D melt column. The left column of graphs show the results calculated for a 50 km melt column, using the partition coefficients of (a) Salters and Longi, (b) La Tourette et al, and (c) Beattie et al (Table 3). The right column of graphs show the results calculated for a 10 km melt column, with the partition coefficients corresponding to those shown on the left. The horizontally trending curves show activity ratios for constant maximum porosity (ϕ_{max}) in percent, while the vertically trending contours show the activity ratios for a constant upwelling rate (W_s) in cm/yr. The bold solid contour in each plot shows a reference upwelling rate of 10 cm/yr, while the bold dashed curve shows a reference maximum porosity of about 1%. Spacing between curves is calculated in log units: increments between curves of solid upwelling rate are $10^{0.2}$ cm/yr, and between curves of constant maximum porosity $10^{0.13}$%. The decrease of (^{231}Pa/^{238}U) and (^{230}Th/^{238}U) at very low upwelling rates is a result of the melting rate approaching the time-scale of the half-lives of ^{231}Pa and ^{230}Th.

Table 4. Calculated melting parameters for Hawaiian plume from ^{238}U-^{230}Th-^{226}Ra from the chromatographic melt transport model.

	Thol (50 km)	AOB (10 km)	Bas (10 km)
Beattie			
ϕ_{max}	0.003	0.001	0.001
W_s (cm/yr)	50	5	3
Salters and Longhi			
ϕ_{max}	0.03	0.01	0.01
W_s (cm/yr)	100	4	1?
La Tourette et al.			
ϕ_{max}	0.02	0.004	0.004
W_s (cm/yr)	40	3	1?
Lundstrom et al.			
ϕ_{max}	0.015	0.005	0.005?
W_s (cm/yr)	40	2	1?
Sims et al. (inverted)			
ϕ_{max}	0.007	0.002	0.002
W_s (cm/yr)	40	2.5	1.5
Range:			
ϕ_{max}	0.3%–3%	0.1%–1%	0.1%–1%
W_s (cm/yr)	40–100	2–5	1–3

Maximum porosity (ϕ_{Max}), and solid mantle upwelling velocity (W_s) calculated from the average ($^{230}Th/^{238}U$) and ($^{226}Ra/^{230}Th$) for the main-stage tholeiites, post-shield alkali basalts and rejuvenated-stage basanites using the Spiegelman and Elliot model (1993) and bulk D_U, D_{Th} and D_{Ra} values given in Table 3. For Beattie, $D_{Ra} = 4 \times 10^{-5}$, for all others we use $D_{Ra} = 1 \times 10^{-5}$. Calculations assume dF/dz = 0.003/km and a 50 km melt column for tholeiitic basalts and 10 km for alkali basalts and basanites. Values marked with ? denote data which fell out of range of the model grids.

the threshold porosity is reached, the porosity of the melt zone is constant. Whereas the Spiegelman and Elliot model is an "infinite Damkohler number" model (melt-solid reaction is very fast relative to melt migration velocity), the dynamic melting model is a "zero-Damkohler number" model. The reality is of necessity somewhere in between (e.g., see Hart, 1993). The dynamic melting model also differs from the Spiegelman and Elliot model in that the trace element enrichments in the melts are intermediate between batch melting and accumulated fractional melting, depending on the value of the threshold porosity relative to the distribution coefficients of the element(s) considered (Williams and Gill, 1989; Zou and Zindler, 1996).

Dynamic melting models (equations given in Appendix I) provide results that are similar to those obtained from the chromatographic porous flow melting model. The extent of ($^{226}Ra/^{230}Th$) disequilibrium is controlled mainly by the porosity of the melt region, and ($^{230}Th/^{238}U$) disequilibrium mainly by the melting rate (Fig. 6). However, with dynamic melting the time-scale of melt migration is not considered. Therefore, for a given set of partition coefficients, the dynamic melting model requires threshold or escape porosities which are lower (about a factor of 1.5) than the maximum porosity at the top of the melt zone predicted by a chromatographic melting model (compare Figs. 4 and 5 with Fig. 6). With dynamic melting, the inferred melting rates are also slightly lower.

In Figure 7, the ($^{230}Th/^{238}U$)-($^{231}Pa/^{235}U$) data are compared to predictions based on batch and accumulated fractional melting models. The results show that the data serve as much to constrain the distribution coefficients as to distinguish between melting models. The data can be adequately fit with a batch melting model (and as shown in Fig. 5 also with the chromatographic porous flow model), using either the experimentally-determined D_U and D_{Th} values of Lundstrom et al. (1994) and LaTourrette (1993) combined with an inferred D_{Pa} value, or the values we derived for the three D values from an inversion of the measured concentration data using the batch melting equations. The data are not well-fit with the accumulated fractional melting model, or if the D_U and D_{Th} values of Beattie (1993a, b) are used.

5. SOURCES OF UNCERTAINTY

The samples collected from historic sub-aerial flows have precisely known and very young ages (Table 1). Uncertainties in the ages of these samples are not significant in assessing the initial isotopic ratios. The Loihi samples are dive or dredge samples collected from submarine surface flows; their ages are estimated to be less than 10,000 years based on measured thicknesses of palagonite rinds. The ages of the Loihi samples are too poorly known to make ^{226}Ra data usable, but the ages are well enough constrained for the ^{230}Th and ^{231}Pa data. Uncertainties in the ^{14}C ages of the prehistoric flows are significant compared to the half-life of ^{226}Ra and are reflected in the large error bars for those samples. The ^{14}C age uncertainties however, are negligible compared to the half-lives of ^{230}Th and ^{231}Pa. Because ^{226}Ra is largely controlled by the porosity of the melt zone, uncertainties in sample ages translate to large uncertainties in the calculated porosity (e.g., see Figs. 4–6).

5.1. Magma Storage Ages

If magma is stored in the crust for significant periods of time before eruption, the parent/daughter activity ratios will decay toward the equilibrium value and cause us to infer too small an amount of parent/daughter fractionation in the melting process. This issue is most significant for ^{226}Ra; it is probably not a significant source of uncertainty for the longer-lived ^{230}Th and ^{231}Pa.

Based on observations and studies of Kilauea volcano, the storage times for tholeiitic basalts erupted during the main stage of volcano growth are probably short. The high magma supply rates (about 0.1 km^3/yr) require that a magma chamber would need to have a volume of 100 km^3 in order for the residence time of magma in the chamber to be as long as 1000 years. Geophysical estimates of the magma volume residing in an upper level reservoir range from 10's to 100's of km^3, indicating a range of residence times: 100's to 1000's of years (Pyle, 1992; Clague, 1996). Other estimates based on thermobarometry (Putirka, 1997) and crystal size distributions (Mangan, 1990) indicate residence times on the order of 10's of years. On the other hand, there are few independent constraints on magma storage times for Hawaiian alkaline lavas. For these lavas, the best limits probably can be derived from the ^{226}Ra data. Assuming that the observed Th-Ra disequilibrium is a result of fractionation produced by melting, the large ($^{226}Ra/^{230}Th$) excesses and the consistency of the values among the samples indicate that magma storage times are probably

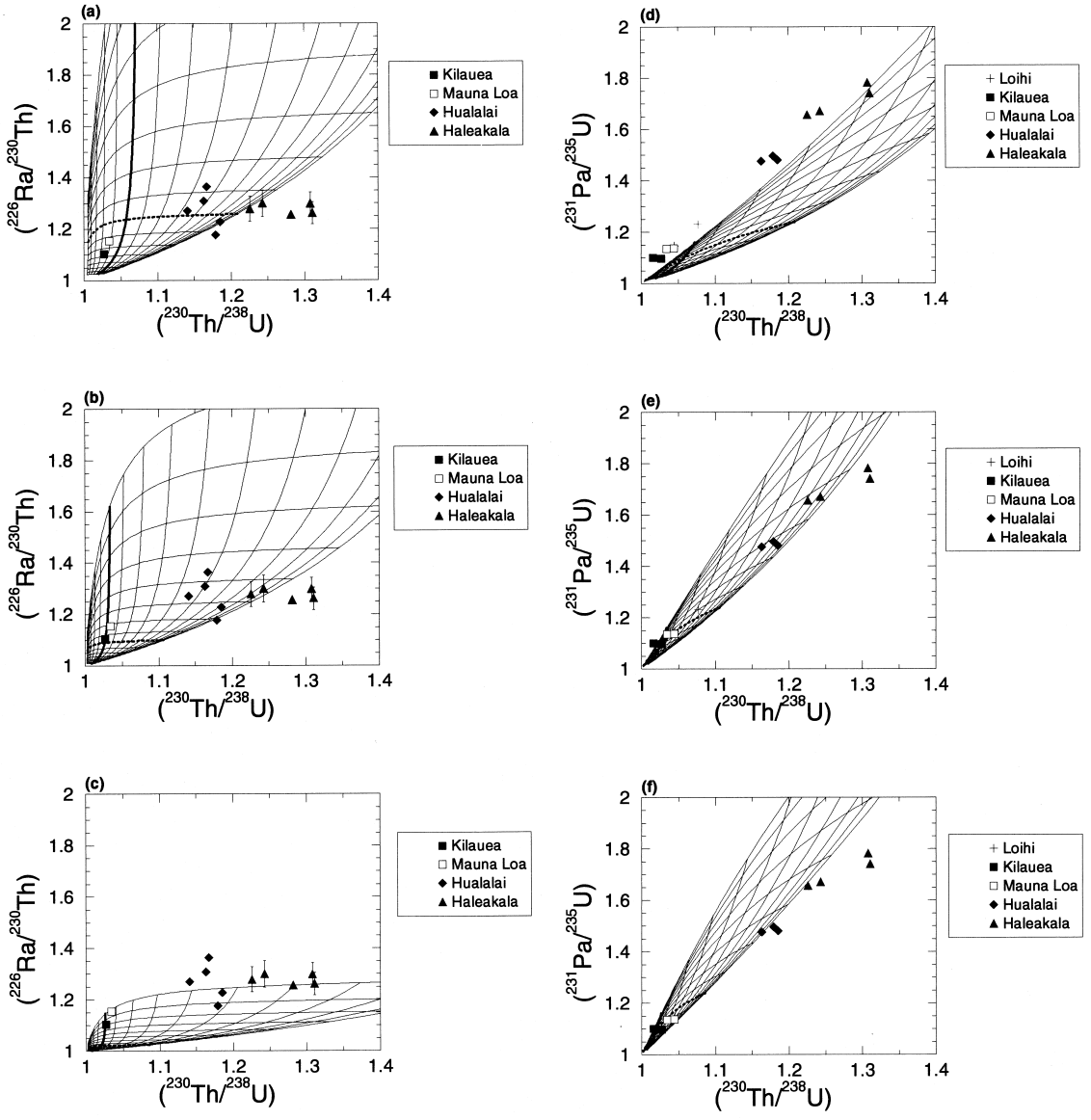

Fig. 6. Comparison of the measured ($^{226}Ra/^{230}Th$) vs. ($^{230}Th/^{238}U$) and ($^{231}Pa/^{238}U$) vs. ($^{230}Th/^{238}U$) for the Hawaiian basalts (symbols) to the calculated values (curves) for dynamic, near-fractional melting through a 1D melt column using the partition coefficients of (a & d) Longi and Salters, (b & e) La Tourette et al, and (c & f) Beattie et al (Table 3). The horizontally trending curves show activity ratios for constant threshold porosity (ϕ_{thres}) in percent, while the vertically trending contours show the activity ratios for a constant upwelling rate (W_s) in cm/yr. The bold solid contour in each plot shows a reference upwelling rate of 10 cm/yr, while the bold dashed curve shows a reference maximum porosity of about 1%. Spacing between curves is calculated in log units: increments between curves of solid upwelling rate are $10^{0.2}$ cm/yr, and between curves of constant maximum porosity $10^{0.13}$%.

much less than one half-life of ^{226}Ra (probably even less than 800 years). Nevertheless, the uncertainties in the storage time limit the interpretation of the ($^{226}Ra/^{230}Th$) data, and must be kept in mind when evaluating the inferred melt zone porosities.

5.2. Uncertainties in Measured U, Th, Ra Partition Coefficients

Calculated porosities and melting rates from both the chromatographic and dynamic melting models are highly dependent upon the absolute and relative values chosen for the U, Th, Pa and Ra partition coefficients (Tables 3 and 4). There are now several experimental measurements of D_U and D_{Th} values for the relevant mantle phases: garnet, clinopyroxene, orthopyroxene, and olivine. While Ra and Pa are thought to be highly incompatible during mantle melting, their absolute D values have never been measured and are only inferred. Based on the fact that Ra and Ba have similar ionic radii (1.40 Å and 1.35 Å) and charge (+2 for both), it is generally assumed that $D_{Ra} \approx D_{Ba}$, which has been measured. For Pa, no experimental mea-

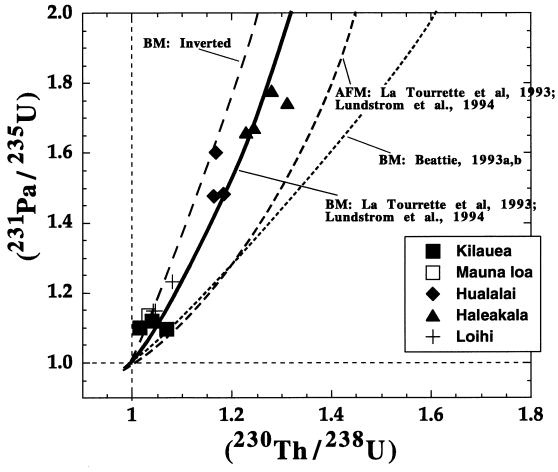

Fig. 7. (^{231}Pa/^{235}U) vs (^{230}Th/^{238}U) for Hawaiian samples compared with static batch melting (BM) and accumulated fractional melting (AFM) of a lherzolite source. The batch melting trends using our inverted D_U-D_{Pa} and D_U-D_{Th} values and the inferred D_{Pa} and the experimentally determined D_U and D_{Th} values from Lundstrom et al. (1994) and La Tourrette (1993) provide a reasonably good fit to the data.

surements have been made and no analogs have been found, therefore it has been generally assumed that the bulk partitioning behavior of Pa is similar to that of U^{5+} (Lundstrom et al., 1995). Another constraint for D_{Pa} comes from measurements of clinopyroxene and coexisting glass, which indicate that D_U/D_{Pa} for clinopyroxene is greater than two (Pickett and Murrell, 1997).

The length of time that the parent element spends in the melt column is critical in the ingrowth models, therefore, these models are most sensitive to the D values chosen for the parent elements U and Th. For the combined U-Th-Ra disequilibria, the value chosen for D_{Th} is particularly important, as ^{230}Th is both a parent and daughter isotope and therefore its D value affects both (^{230}Th/^{238}U) and (^{226}Ra/^{230}Th) disequilibria. In the above modeling it is also assumed that the U-Th-Ra partitioning is controlled by major phases (olivine, pyroxene and garnet) and that partitioning of U, Th, Pa and Ra between the melt and solid is constant throughout the melting column. While it can be reasoned that the partitioning of U, Th, (and Ra and Pa?) is controlled by the major mantle phases (Beattie, 1993a, b; La Tourrette et al., 1993) it has been recently shown that the values of mineral/melt partition coefficients can be highly dependent on the chemical compositions of the minerals as well as the temperature and pressure of the experiments. In fact, recent high-pressure experiments show that D_U and D_{Th} values can vary by as much as a factor of 10 due to variations in mineral composition and pressure (Beattie, 1993a, b; La Tourrette, 1993; Lundstrom et al., 1994; Salters and Longhi, 1999). The large variations between the different experimentally determined D_U and D_{Th} values for clinopyroxene and garnet (Table 3) result in large variations in the calculated porosities and melting rates for both chromatographic and dynamic melting models (Table 4). Until these issues are resolved and the effect of chemical composition, temperature and pressure on the measured partitioning values for U, Th, (and Pa and Ra) are established, calculated solid mantle upwelling rates and porosities based upon (^{230}Th/^{238}U) (^{226}Ra/^{230}Th) and (^{231}Pa/^{235}U) disequilibria must be considered as preliminary estimates only.

6. Th/U SOURCE RATIOS: CORRELATION BETWEEN ^{230}Th/^{232}Th AND ^{87}Sr/^{86}Sr AND ^{143}Nd/^{144}Nd

Because the upwelling rates in Hawaii are large and the ingrowth of ^{230}Th during melting is relatively small compared to the net elemental fractionation of U/Th, the (^{230}Th/^{232}Th) ratio can be used to characterize the mantle magma source of basalts in much the same way the ^{87}Sr/^{86}Sr and ^{143}Nd/^{144}Nd are used. There is one significant difference: the ^{87}Sr/^{86}Sr and ^{143}Nd/^{144}Nd ratios reflect the Rb/Sr and Sm/Nd of the mantle integrated over time-scales of 10^9 years, whereas the ^{230}Th/^{232}Th gives information on the ^{238}U/^{232}Th ratio of the mantle source integrated only over about 5×10^5 years. Nevertheless, for both the Hawaiian and MORB data there are similarities between the U-Th, Sm-Nd and Rb/Sr systems (Figs. 8a and 8b). The Hawaiian samples have ε_{Nd}, ^{87}Sr/^{86}Sr and (^{230}Th/^{232}Th) values which are between those of MORB and CHUR; the post-caldera and post-erosional alkali basalts and basanites have higher, more MORB-like values than the pre-shield and shield stage tholeiites and alkali basalts (except for the (^{230}Th/^{232}Th) of Hualalai). The correlation between the Th isotopic data and the Sr and Nd isotopic data suggest that the inferred Th/U ratios are also a long-lived feature of the magma sources (cf. Allegre and Condomines, 1982).

7. VARIATIONS IN SOLID MANTLE UPWELLING AND THE STRUCTURE OF THE HAWAIIAN MANTLE PLUME

Using a model for Hawaiian volcano growth from DePaolo and Stolper (1996), we have calculated the radial position of the volcanoes relative to the center of the Hawaiian plume, which allows us to make a crude "map" of upwelling rates in the Hawaiian plume (Fig. 9). The center of the plume is located so that the active volcanoes Loihi, Kilauea and Mauna Loa are positioned appropriately for their model ages and eruption rates (see inset Fig. 9). The pattern in calculated upwelling rate relative to radial distance from the plume axis is shown in Figure 9, where it is also compared to the fluid dynamical models of Watson and McKenzie (1991) and Hauri et al. (1994). The values inferred from the isotopic data are reasonably consistent with the Watson and McKenzie (1991) model near the fringes of the plume and considerably lower than the Hauri et al. (1994) model values. For Kilauea and Mauna Loa, the inferred upwelling velocities are probably representative of the core of the plume, and these are closer to the Hauri et al. values (1994) than they are to the Watson and McKenzie (1991) model values. These estimates will need to be refined with more accurate values of distribution coefficients and better models for the melt productivity, but they illustrate that the U-series disequilibrium isotopic data may provide a much-needed constraint on the dynamics of the plume.

8. COMMENTS ON THE POROSITY OF THE MELT ZONE AND MELT TRANSPORT TIMES

In the dynamic melting model, the U-series disequilibria are produced at the bottom of the melt column and the melt is transported to the surface rapidly, relative to the half-life of the

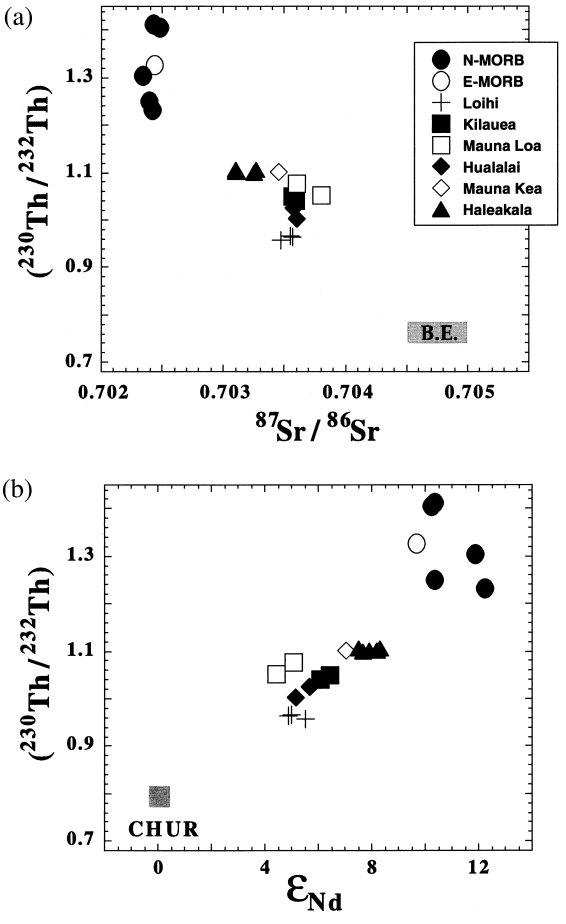

Fig. 8. **a.** (^{230}Th/^{232}Th) vs ^{87}Sr/^{86}Sr and **b.** (^{230}Th/^{232}Th) vs ε_{Nd} for the Hawaiian basalts. MORB data from Goldstein et al., 1994; Sims et al., 1995.

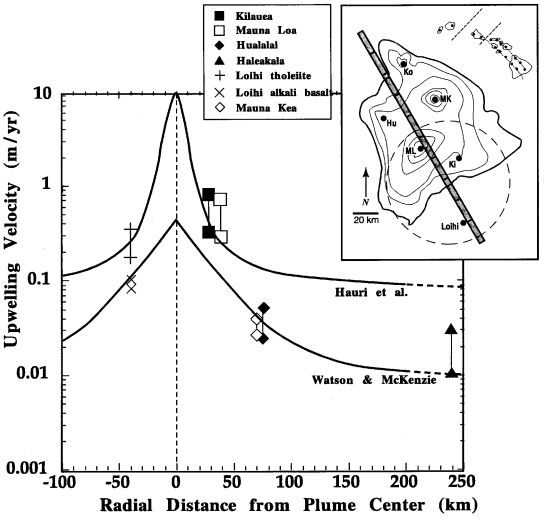

Fig. 9. Solid mantle upwelling rate calculated from ^{238}U-^{230}Th-^{226}Ra and ^{235}U-^{231}Pa disequilibria versus the radial position of the volcanoes relative to the center of the Hawaiian plume. The center of the plume (see inset) is located so that the active volcanoes Loihi, Kilauea and Mauna Loa are positioned appropriately for their model ages and eruption rates (DePaolo and Stolper, 1996). Also shown are the model curves for solid mantle upwelling from Watson and McKenzie (1991) and Hauri et al. (1994). The model of Watson and McKenzie (1991) assumes a constant viscosity across the plume whereas the Hauri et al. model incorporates a temperature-dependent viscosity.

shortest lived isotope (in this case ^{226}Ra). With the chromatographic melting model, the time-scale of melt migration is taken into account and the velocity of the melt can be determined explicitly (Appendix I, Eqn. 6). Since the analytical solutions assume a constant porosity the melt velocities are also constant throughout the melting column. With the numerical solution, melt velocity varies as a function of the porosity distribution of the melt column. In this case, it is more useful to calculate melt transport times by integrating the melt velocity over the length of the melt column.

Here we determine the melt transport times for the Hawaiian magmas using the porosity distribution given in Appendix I. Assuming a 50 km melt column for the tholeiitic basalts and a 10 km melt column for the alkali basalts and basanites and using the range of maximum porosities (ϕ_{Max}) and solid mantle upwelling rates (W_S) given in Table 4, we calculate melt transport times of 1.5 to 32 ka for tholeiites, 2 to 50 ka for the alkali basalts and 4 to 100 ka for the basanites. Because of the different column lengths, these transport times indicate that the tholeiites are moving up to 5 times faster than the alkali basalts and basanites, which is consistent with higher melting rates in the central plume.

9. CONCLUSIONS

1. (^{230}Th/^{238}U), (^{226}Ra/^{230}Th), (^{231}Pa/^{235}U) disequilibria in Hawaiian basalts vary systematically with major-element chemistry and Sm/Nd fractionation.
2. There have now been several experimental determinations of U and Th partition coefficients for clinopyroxene and garnet (Table 3); the observation that (^{230}Th/^{238}U) >1 in all of these samples indicates that garnet is required as a residual phase in their magma sources. To date, there have not been any actual experimental determinations of Ra and Pa mineral/melt partition coefficients for mantle phases, and therefore, (^{231}Pa/^{235}U) and (^{226}Ra/^{230}Th) do not presently place constraints on the mineralogy of the source or the depth of melting.
3. The (^{230}Th/^{238}U) and (^{231}Pa/^{235}U) disequilibria in these Hawaiian basalts, because of the relatively long half-lives of ^{230}Th and ^{231}Pa, can be modeled in terms of batch melting. This suggests that much of the U/Th and U/Pa disequilibria result from net U/Th and U/Pa elemental fractionations during melting.
4. The (^{226}Ra/^{230}Th) disequilibria because of the much shorter half-life of ^{226}Ra, require "ingrowth" models which treat explicitly the time scales of melt generation and melt extraction.
5. The combined (^{230}Th/^{238}U), (^{226}Ra/^{230}Th), (^{231}Pa/^{235}U) disequilibria and the observed range in major- and trace-element chemistry of these lavas can be understood in terms of variations in the melting parameters, porosity and upwelling rate (related to solid mantle upwelling rate), as the volcanoes, carried by the moving pacific plate, traverse the Hawaiian plume.

6. ($^{226}Ra/^{230}Th$) and other geochemical, geophysical, petrological and field evidence suggest relatively short magma storage times for all of these lavas ($<t_{1/2}$ ^{226}Ra), with the exception of the Mauna Kea samples which are evolved Hawaiites.
7. ($^{230}Th/^{232}Th$) in the Hawaiian basalts co-varies with both ε_{Nd} and $^{87}Sr/^{86}Sr$. This variation can be understood in terms of two-component mixing of a more depleted and more enriched source.

Acknowledgments—This paper is dedicated to the memory of RW Sims. Conversations with Ed Sklar, Peter Kelemen, Stan Hart, and Greg Hirth are greatly appreciated. Formal and informal reviews from Mark Spiegelman, Vincent Salters, Tim Elliot, Aaron Petruzska, Craig Lundstrom, Ken Rubin have improved the quality and accuracy of this manuscript. Support for this research was provided by: a WHOI postdoctoral fellowship (KWWS), a grant from Institute of Geophysics and Planetary Physics at Los Alamos National Laboratory (KWWS, DJP, MTM) and from Basic Energy Science, U.S. Department of Energy (MM, SG).

REFERENCES

Allegre, C. J. and Condomines M. (1982) Basalt genesis and mantle structure studied through Th-isotopic geochemistry. *Nature* **299,** 21–24.

Asimov, P. D., Hirschmann, M. M., and Stolper, E. M. (1997) An analysis of variations in isentropic melt productivity. *Phil. Trans. R. Soc. Lond. A* **355,** 255–281.

Beattie, P. (1993a) Uranium-thorium disequilibria and partitioning on melting of garnet peridotite. *Nature* **363,** 63–65.

Beattie, P. (1993b) The Generation of uranium series disequilibria by partial melting of spinel peridotite: constraints from partitioning studies. *Earth Planet. Sci. Lett.* **117,** 379–391.

Ben Othman, D. and Allegre C. J. (1990) U-Th isotopic systematics at 13° N east Pacific Ridge segment. *Earth Planet. Sci. Lett.* **98,** 129–137.

Bourdon, B., Zindler, A., Elliott, T. and Langmuir, C. (1996) Constraints on mantle melting at mid-ocean ridges from global ^{238}U-^{230}Th disequilibrium data. *Nature* **384,** 231–235.

Blundy, J. D. and Wood, B. J. (1994) Prediction of crystal-melt partition coefficients from elastic moduli. *Nature* **373,** 452–454.

Chabaux, F., Othman, D. B., and Birck, J. L. (1994) A new Ra-Ba chromatographic separation and its application to Ra mass-spectrometric measurement in volcanic rocks. *Chem. Geo.* **114,** 191–197.

Chabaux, F. and Allegre, C. J. (1994) ^{238}U-^{230}Th-^{226}Ra disequilibria in volcanics: A new insight into melting conditions. *Earth Planet. Sci. Lett.* **126,** 61–74.

Clague, D. A. (1996) Crustal compositions that modify hot-spot magma compositions: Kilauea Volcano, Hawaii, Am. Geophys. U Chapman Conference "Shallow level processes in ocean island magmatism" 20–21.

Clague, D. A. (1987) Hawaiian alkaline volcanism, in *Alkaline Igneous Rocks*, J. G. Fitton and B. G. J. Upton (eds), *GSA Spec. Publ.* **30,** 227–252.

Crandell, D. R. (1983) Potential hazards from future volcanic eruptions on the island of Maui, Hawaii, Miscellaneous investigations series Map I-1442, USGS.

Condomines, M., Morand, P., and Allegre, C. J. (1988) ^{230}Th-^{238}U radioactive disequilibria in tholeiites from the FAMOUS zone (Mid-Atlantic Ridge, 36°50′N): Th and Sr isotopic geochemistry. *Earth Planet. Sci. Lett.* **55,** 247–256.

Condomines, M., Hemond, Ch., and Allegre, C. J. (1988) U-Th-Ra radioactive disequilibria and magmatic processes. *Earth Planet. Sci. Lett.* **90,** 243–262.

Cohen, A. S. and O'Nions, R. K. (1991) Precise Determination of Femtogram Quantities of Radium by Thermal Ionization Mass Spectrometry. *Anal. Chem.* **63,** 2705–2708.

Cohen, A. S. and O'Nions, R. K. (1993) Melting rates beneath Hawaii: Evidence from uranium series isotopes in recent lavas. *Earth Planet. Sci. Lett.* **120,** 169–175.

Condomines, M. (1994) Comment on: "The volume and residence time of magma beneath active volcanoes determined by decay-series disequilibria methods". *Earth Planet. Sci. Lett.* **122,** 251–255.

Condomines, M., Hemmond, Ch., and Allegre, C. J. (1988) U-Th-Ra disequilibria and magmatic processes. *Earth Planet. Sci. Lett.* **90,** 243–263.

DePaolo, D. J. (1988) *Neodymium Isotope Geochemistry*. Springer-Verlag.

DePaolo, D. J. (1996) High-frequency isotopic variations in the Mauna Kea tholeiitic basalt sequence: Melt zone dispersivity and chromatography. *J. Geophys. Res.* **101,** 11,855–11,864.

DePaolo, D. J. and Stolper, E. M. (1996) Models of Hawaiian volcano growth and plume structure: implications of results from the Hawaii Scientific Drilling Project. *J. Geophys. Res.* **101,** 11,643–11,654.

Elliot, T. (1997) Fractionation of U and Th during mantle melting: a reprise. *Chem. Geology*, 139.

Forsyth, D. W. (1992) Geophysical constraints on mantle flow and melt generation beneath mid-ocean ridges, in *Mantle Flow and Melt Generation at Mid-Ocean Ridges*, J. P. Morgan, D. K. Blackman and J. M. Sinton (eds), *Geophysical Monograph* **71,** Am. Geophys. Union.

Frey, F. A. and Clague D. A. (1983) Geochemistry of diverse basalt types from Loihi Seamount, Hawaii: petrogenetic implications. *Earth Planet. Sci. Lett.* **66,** 337.

Goldstein, S. J., Murrell, M. T., and Janecky, D. R. (1989) Th and U isotopic systematics of basalts from the Juan de Fuca and Gorda ridges by mass spectrometry. *Earth Planet. Sci. Lett.* **96,** 134–146.

Goldstein, S. J., Murrell, M. T., Janecky, D. R., Delaney, J. R., and Clague, D. A. (1992) Geochronology and petrogenesis of MORB from the Juan de Fuca and Gorda Ridges by ^{238}U-^{230}Th disequilibrium. *Earth Planet. Sci. Lett.* **109,** 255–272.

Green, D. H. (1970) A review of experimental evidence on the origin of basaltic and nepheleneitic magmas. *Phys. Earth Planet. Inter.* **3,** 221–235.

Hart, S. R. (1993) Equilibration during mantle melting: A fractal tree model. *Proc. Natl. Acad. Sci.* **90,** 11914–11918.

Hauri, E. H., Whitehead, J. A., and Hart, S. R. (1994) Fluid dynamic and geochemical aspects of entrainment in mantle plumes. *Jour. Geophys. Res.* **99,** 24,275–24,300.

Hemmond, C., Hofmann, A. W., Heusser, G., Condomines, M., Raczek, I., and Rhodes M. J. (1994) U-Th-Ra systematics in Kilauea and Mauna Loa basalts, Hawaii. *Chem. Geol.* **116,** 163–180.

Hon, K., Kauakikaua, J., Denlinger, R., and Mackay, K. (1994) Emplacement and inflation of pahoehoe sheet flows: observations and measurements of active lava flows on Kilauea Volcano, Hawaii. *Geol. Soc. Am. Bull.* **106,** 351–379.

Iwamori, H. (1994) ^{238}U-^{230}Th-^{226}Ra and ^{235}U-^{231}Pa disequilibria by mantle melting with porous and channel flows. *Earth Planet. Sci. Lett.* **125,** 1–16.

Kushiro, I. (1980) Viscosity, density, and structure of silicate melts at high pressures, and their petrological applications. In *Physics of Magmatic Processes*, R. B. Hargraves (ed) Princeton University Press, 93–121.

LaTourrette, T. Z. and Burnett, D. S. (1992) Experimental determination of U and Th during partitioning between clinopyroxene and natural and synthetic basalt liquid. *Earth Planet Sci. Lett.* **110,** 227–244.

LaTourrette, T. Z., Kennedy, A. K., and Wasserburg, G. J. (1993) U-Th fractionation by garnet-evidence for a deep source and rapid rise by oceanic basalts. *Science* **261,** 739–742.

Lockwood, J. P., Lipman, P. W., Petersen, L. D., and Warshauer, F. R. (1988) Generalized ages of surface lava flows of Mauna Loa volcano, Hawaii, Miscellaneous investigations series Map I-1908, USGS.

Lundstrom, C. C., Shaw, H. F., Ryerson, F. J., Phinney, D. L., Gill, J., and Williams, Q. (1994) Compositional controls on the partitioning of U, Th, Ba, Pb, Sr, and Zr between clinopyroxene and haplobasaltic melts: implications for U-series disequilibria in basalts. *Earth Planet. Sci. Lett.* **128,** 407–423.

Lundstrom, C. C., Gill, J., Williams Q., and Perfit, M. R. (1995) "Mantle Melting and Basalt Extraction by Equilibrium Porous Flow". *Science* **270,** 1958–1961.

Managan, M. T. (1990) Crystal size distribution and the systematics of magma storage times: The 1959 eruption of Kilauea volcano, Hawaii. *J. Volcan. Geothermal. Res.* **44,** 295–302.

McKay, G. A. (1989) Partitioning of REE between major silicate minerals and basaltic melts, in *Geochemistry and Mineralogy of*

REE, B. R. Lipin and G. A. McKay (eds), *Reviews in Mineralogy*, vol 21, 45–75.
McKenzie, D. (1984) The generation and compaction of partially molten rock. *J. Petrol.* **25,** 713–765.
McKenzie, D. (1985) ^{230}Th-^{238}U disequilibrium and the melting processes beneath ridge axes. *Earth Planet. Sci. Lett.* **72,** 149–157.
McKenzie, D. (1989) Comments on small melt fractions. *Earth Planet. Sci. Lett.* **95,** 53–72.
McKenzie, D. and Bickle, M. J. (1988) The volume and composition of melt generated by extension of the lithosphere. *J. Petrol.* **29,** 625–679.
Moore, R. B. and Clague, D. A. (1981) Geologic map of Hualalai volcano, Hawaii, Miscellaneous investigations series Map I-2213, USGS.
Moore, R. B., Clague, D. A., and Normark, W. R. (1982) Diverse basalt types from Loihi Seamount, Hawaii. *Geology* **10,** 88.
Newman, S., Finkel, R. C., and Macdougall, J. D. (1983) ^{230}Th-^{238}U disequilibrium systematics in oceanic tholeiites from 21°N on the East Pacific Rise. *Earth Planet. Sci. Lett.* **65,** 17–33.
Oostdam, B. L. (1965) Age of lava flows on Haleakala, Maui, Hawaii. *Geol. Soc. America Bull.* **76,** 393–394.
Pickett, D. A., Murrell, M. T., and Williams, R. W. (1994) Determination of femtogram quantities of Pa in geological samples by thermal ionization mass spectrometry. *Anal. Chem.* **66,** 1044–1049.
Pickett, D. A. and Murrell, M. T. (1997) Observations of ^{231}Pa/^{235}U disequilibrium in volcanic rocks. *Earth Planet. Sci. Lett.* **148,** 259–271.
Porter, S. C. (1979) Quaternary stratigraphy and chronology of Mauna Kea, Hawaii: A 380,000 year record of mid-Pacific volcanism and ice-cap glaciation: Summary. *Geol. Soc. Am. Bull.* **90,** 609–611.
Putirka, K. (1997) Magma transport at Hawaii: inferences based on igneous thermobarometry. *Geology* **25,** 69–72.
Pyle, D. M. (1992) The volume and residence time of magma beneath active volcanoes determined by decay series disequilibria methods. *Earth Planet. Sci. Lett.* **112,** 61–73.
Qin, Z. (1992) Disequilibrium partial melting model and its implications for trace element fractionations during mantle melting. *Earth Planet Sci. Lett.* **112,** 75–90.
Qin, Z. (1993) Dynamics of melt generation beneath mid-ocean ridge axes: Theoretical analysis based on ^{238}U-^{230}Th-^{226}Ra and ^{235}U-^{231}Pa disequilibria. *Geochim. Cosmochim. Acta* **57,** 1629–1634.
Reber, G. (1959) Age of lava flows on Haleakala, Hawaii. *Geol. Soc. America Bull.* **70,** 1245–1246.
Ribe, N. M. (1985) The generation and composition of partial melt in the earth's mantle. *Earth Planet. Sci. Lett.* **73,** 361–376.
Ribe, N. M. (1987) Theory of melt segregation—a review. *Journ. of Volcan. and Geotherm. Res.* **33,** 241–253.
Ribe, N. M. (1988) Dynamical geochemistry of the Hawaiian plume. *Earth Planet. Sci. Lett.* **88,** 37–46.
Rienitz, I. and Turekian, K. K. (1989) ^{230}Th/^{238}U and ^{226}Ra/^{230}Th fractionation in young basaltic glasses from the East Pacific rise. *Earth Planet. Sci. Lett.* **94,** 199–207.
Richardson, C. and McKenzie, D. (1994) Radioactive disequilibria from 2D models of melt generation by plumes and ridges. *Earth Planet. Sci. Lett.* **128,** 425–437.
Richter, F. M. and McKenzie, D. (1984) Dynamical models for melt segregation from a deformable matrix. *J. of Geol.* **92,** 729–740.
Rubin, K. H. and Macdougall, J. D. (1988) ^{226}Ra excesses in mid-ocean ridge basalts and mantle melting. *Nature* **335,** 158–161.
Salters, V. J. M. and Longhi, J. E. (1999) Trace-element partitioning during the initial stages of melting beneath mid-ocean ridges. *Earth Planet Sci. Lett.* **166,** 15–30.
Sims, K. W. W., DePaolo, D. J., Murrell, M. T., Baldridge, W. S., Goldstein, S. J., and Clague, D. A. (1995) Mechanisms of magma generation beneath Hawaii and mid-ocean ridges: U/Th and Sm/Nd isotopic evidence. *Science* **267,** 508–512.
Spiegelman, M. and Elliot, T. (1993) Consequences of melt transport for U-series disequilibrium in young lavas. *Earth Planet. Sci. Lett.* **118,** 1–20.
Spiegelman, M. and Kenyon, P. (1992) The requirements for chemical disequilibrium during magma migration. *Earth Planet. Sci. Lett.* **109,** 611–620.
Stolper, E., Walker, D., Hager, B. H., and Hays, J. F. (1981) Melt segregation from partially molten source regions: the importance of melt density and source region size. *J. Geophys. Res.* **86,** 6261–6271.
Turcotte, D. L. (1982) Magma migration. *Ann. Rev. Earth Planet. Sci.* **10,** 397–408.
Volpe, A. M., Olivares, J. A., and Murrell, M. T. (1991) Determination of Radium Isotope Ratios and Abundances in Geologic Samples by Thermal Ionization Mass Spectrometry. *Anal. Chem.* **63,** 913–916.
Watson, S. and McKenzie, D. (1991) Melt Generation by Plumes: A Study of Hawaiian Volcanism. *J. Pet.* **32,** 501–537.
Williams, R. W. and Gill, J. B. (1989) Effects of partial melting on the uranium decay series. *Geochim. Cosmochim Acta* **53,** 1607–1619.
Zou, H. and Zindler, A. (1996) Constraints on the degree of dynamic partial melting and source composition using concentration ratios in magmas. *Geochem. Cosmochim. Acta* **60,** 711–717.

APPENDIX 1

A. Chromatographic Melt Transport: Analytic Approximations of the Numerical Solution

Following the approach of Spiegelman and Elliot (1993), the effects of transport of melt through a melting column on the chemistry of radiogenic isotopes can be separated from melting by expressing the concentration of an element as

$$c_i = \alpha_i c_{bi} \tag{1}$$

where c_i is the concentration of an element measured at the surface, c_{bi} is the concentration of a stable element due to batch melting and α_i is the enrichment factor due to transport. The concentrations in the melt are given by the batch melting equation, despite the fact that the porosity is small and the melt moves relative to the solid, because of the assumption of continuous re-equilibration of solid and liquid. Fractional melts are produced only if the solid does not re-equilibrate with the melt that passes through it (see Appendix of Spiegelman and Elliot (1993)).

For the decay chain ^{238}U-^{230}Th-^{226}Ra, the change in α_i with position in a 1D melt column for each isotope can be expressed by the following (Note that in equation (15) of Spiegleman and Elliot (1993) there is a typographical error)

$$\frac{d\alpha_0}{d\zeta} = -\lambda_0\tau_0\alpha_0 \tag{2}$$

$$\frac{d\alpha_1}{d\zeta} = \lambda_1(\tau_0\alpha_0 - \tau_1\alpha_1) \tag{3}$$

$$\frac{d\alpha_2}{d\zeta} = \lambda_2(\tau_1\alpha_1 - \tau_2\alpha_2) \tag{4}$$

where ζ is the dimensionless distance (z/d) along a column of length d, λ_i are the decay constants ($\ln(2)/t_{1/2}$), and $\tau_i = d/w^i_{eff}$ is the effective transport time of an element along the column. The effective velocity is given by

$$w^i_{eff} = \frac{\rho_f\phi w + \rho_s(1-\phi)D_i W}{\rho_f\phi + \rho_s(1-\phi)D_i} \tag{5}$$

where ρ_f and ρ_s are the melt and solid densities, respectively, ϕ is the porosity, w is the melt velocity, W is the solid upwelling velocity, and D_i is the bulk partition coefficient. Note that if the partition coefficient D_i is $\ll 1$, the effective velocity approaches the melt velocity, and also that the difference in effective velocity between elements with different D_i decreases at larger porosities. In the following text, the subscripts 0, 1, and 2 are taken to refer to ^{238}U, ^{230}Th, and ^{226}Ra, respectively.

Equations (2–4) form a coupled system of differential equations, whereby the decay of each parent can increase the concentration of the daughter element as melt migrates through the melting region. To solve these equations for the enrichment factor α_i, we can make the problem analytically tractable by assuming that both the melt velocity (w) and porosity (ϕ) remain constant over the melt column, using only their average values. (It should be emphasised that the assumption of constant porosity is made with reference to the migration of melt only, and that for the purposes of melting of the solid matrix, the melt fraction at

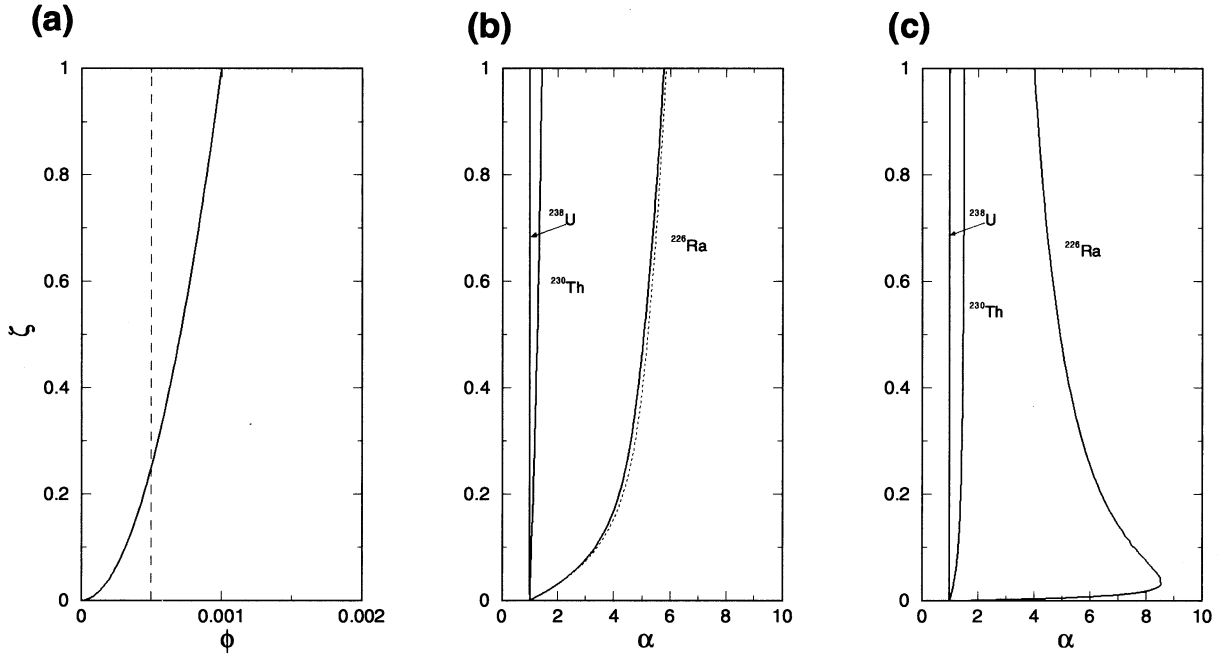

Fig. A1. a) Porosity distribution (ϕ) for a 1D melt column (solid curve) assuming constant melt flux (see Spiegelman and Elliot, 1993). Average porosity is shown as the dashed line. b) Enrichment factors (α) calculated from the analytical solution (solid curves) and approximate analytical solution (dotted curves) for ^{238}U, ^{230}Th and ^{226}Ra. c) Enrichment factors (α) calculated from the numerical solution of Spiegelman and Elliot (1993) for ^{238}U, ^{230}Th and ^{226}Ra. In these plots depth (ζ) is non-dimensionalized. See text for explanation.

the solidus is zero and increases linearly upwards.) For a 1D steady-state melting column, the average melt velocity is given by

$$w = \frac{\Gamma d}{\rho_l \phi 2} \tag{6}$$

where Γ is the melting rate, which we assume to be constant, and is given by

$$\Gamma = \frac{W \rho_s F_{\max}}{d} \tag{7}$$

Solving equations (2–4), we obtain

$$\alpha_0(\zeta) = \alpha_0^o e^{-\lambda_0 \tau_0 \zeta} \tag{8}$$

$$\alpha_1(\zeta) = \frac{\lambda_1 \tau_0 \alpha_0^o}{\lambda_1 \tau_1 - \lambda_0 \tau_0} e^{-\lambda_0 \tau_0 \zeta} + \left[\alpha_1^o - \frac{\lambda_1 \tau_0 \alpha_0^o}{\lambda_1 \tau_1 - \lambda_0 \tau_0} \right] e^{-\lambda_1 \tau_1 \zeta} \tag{9}$$

$$\alpha_2(\zeta) = \frac{\lambda_2 \lambda_1 \tau_1 \tau_0 \alpha_0^o}{(\lambda_1 \tau_1 - \lambda_0 \tau_0)(\lambda_2 \tau_2 - \lambda_0 \tau_0)} e^{-\lambda_0 \tau_0 \zeta} + \frac{\lambda_2 \tau_1}{\lambda_2 \tau_2 - \lambda_1 \tau_1} \left[\alpha_1^o - \frac{\lambda_1 \tau_0 \alpha_0^o}{\lambda_1 \tau_1 - \lambda_0 \tau_0} \right] e^{-\lambda_1 \tau_1 \zeta} + \left[\alpha_2^o - \frac{\lambda_2 \lambda_1 \tau_1 \tau_0 \alpha_0^o}{(\lambda_1 \tau_1 - \lambda_0 \tau_0)(\lambda_2 \tau_2 - \lambda_0 \tau_0)} - \frac{\lambda_2 \tau_1}{\lambda_2 \tau_2 - \lambda_1 \tau_1} \left(\alpha_1^o - \frac{\lambda_1 \tau_0 \alpha_0^o}{\lambda_1 \tau_1 - \lambda_0 \tau_0} \right) \right] e^{-\lambda_2 \tau_2 \zeta} \tag{10}$$

where α_0^o, α_1^o, and α_2^o are constants of integration. For secular equilibrium at the base of the melting column, we set $\alpha_i^o = 1$.

Figure A1(a) shows the constant value of porosity used in the analytic model (dashed curve), compared to the porosity distribution for a 1D melt column in which the upward flux of melt is required to remain constant (see Spiegelman and Elliot, 1993). The solid curves in Figure A1(b) show values of α_i calculated from equations (8–10) along the (dimensionless) length of the melting column for the ^{238}U decay chain with a constant porosity of .1% and solid upwelling velocity of 1 cm/yr. Figure A1(b) also shows the values of α_i (dashed curves) calculated from the solution

$$\alpha_0(\zeta) = \alpha_0^o e^{-\lambda_0 \tau_0 \zeta} \tag{11}$$

$$\alpha_1(\zeta) = \alpha_1^o e^{-\lambda_1 \tau_1 \zeta} + \frac{\tau_0}{\tau_1} \alpha_0 [1 - e^{-\lambda_1 \tau_1 \zeta}] \tag{12}$$

$$\alpha_2(\zeta) = \alpha_2^o e^{-\lambda_2 \tau_2 \zeta} + \frac{\tau_1}{\tau_2} \alpha_1 [1 - e^{-\lambda_2 \tau_2 \zeta}] \tag{13}$$

which was obtained by solving equations (3) and (4) while holding the values of α_0 and α_1 held constant, respectively. This is equivalent to saying that the change in α for a given daughter isotope over the melt column is large compared to that of the parent element. It is evident in Figure A1(b) that this approximate analytical solution is nearly identical to the full analytic solution. The reason for this can be seen by considering the terms $\lambda_0 \tau_0$, $\lambda_1 \tau_1$, and $\lambda_2 \tau_2$, in the full analytic solution (equations 8–10), which represent the ratio of the effective transport time with the time taken for concentration of the isotope to decrease by half. For ^{238}U, $e^{-\lambda_0 \tau_0 \zeta} \approx 1$, while for ^{226}Ra, $e^{-\lambda_2 \tau_2 \zeta} \approx 0$. With these approximations, α_1 in equations (9) and (12) are identical, and this is evident in Figure A1(b). For α_2, equation (10) reduces to equation (13) if $\lambda_1 \tau_1 \ll \lambda_2 \tau_2$, which is nearly true for ^{230}Th and ^{226}Ra. Therefore, perhaps surprisingly, for the ^{238}U decay chain, the system of ordinary differential equations (2–4) can essentially be treated as if they are decoupled. Figure A1(c) shows the full numerical solution for α of Spiegelmen and Elliot (1993). It is evident that in comparison of A1(c) with A1(b), the numerical and analytic solutions differ significantly, with the analytic solution overestimating ($^{226}Ra/^{230}Th$). In Figure A2, comparison of the activity ratios calculated from the full analytic solution (light solid curves), the approximate analytic solution (light dotted curves), and the full numerical solution (dark solid curves) is shown for ($^{226}Ra/^{230}Th$) and ($^{230}Th/^{238}U$) using a melt column of 50 km and total melt fraction of 15% and constant partition coefficients from Lundstrom et al. (1994) for garnet peridotite. The maximum porosity for the melt column is varied from .1–10% and the solid upwelling velocity is varied from 1–100 cm/yr. It is clear that there is a major difference between the analytic and numerical solutions. Considering that ($^{226}Ra/^{230}Th$) is controlled mainly by the porosity, while

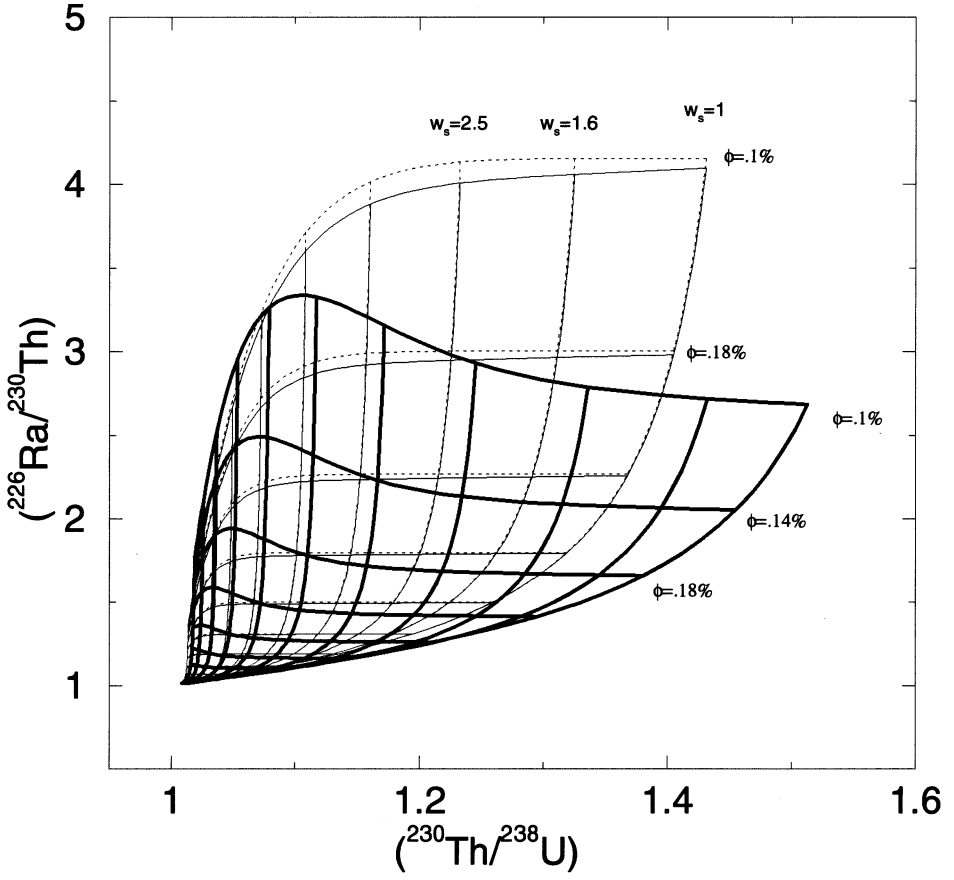

Fig. A2. (^{226}Ra/^{230}Th) and (^{230}Th/^{238}U) calculated from the analytical solution (solid light curves), approximate analytical solution (dotted light curves) and full numerical solution (solid dark curves). Horizontal curves represent constant maximum porosity (ϕ_{max}), while vertical curves represent constant upwelling rates (W_s) in cm/yr. Selected contours are labeled. Contours range from 1–100 cm/yr and 0.1–10% for upwelling velocity and maximum porosity, respectively. See text for explanation.

($^{230}Th/^{238}U$) is controlled mainly by the upwelling rate, it can concluded that the analytic solution overestimates the porosity and underestimates the upwelling velocity.

From the results in Figure A2, it is not clear that the analytic solution using the average porosity and melt velocity does a very good job at approximating the numerical solution. Both the ($^{226}Ra/^{230}Th$) and ($^{230}Th/^{238}U$) values are significantly different from the numerical solution, indicating the importance of taking into consideration the details of the porosity distribution and melt velocity along the melt column.

B. Dynamic Melt Transport

The expressions for the production of ^{238}U-^{230}Th-^{226}Ra disequilibria during dynamic melting (near fractional) were first derived by McKenzie (1985) and have subsequently been presented in several papers pertaining to the production of U-series disequilibria in basaltic melts (Williams and Gill, 1989; Beattie, 1993a; Chaubux and Allegre, 1994).

Assuming a constant melt rate (Γ), by mass, and porosity (ϕ), the ($^{230}Th/^{238}U$) and ($^{226}Ra/^{230}Th$) can be expressed as a function of ϕ and Γ:

$$\left(\frac{^{230}Th}{^{238}U}\right) = \frac{F_{Th}(K_U + \lambda_{Th})}{F_U(K_{Th} + \lambda_{Th})} \tag{14}$$

$$\left(\frac{^{226}Ra}{^{230}Th}\right) = \frac{F_{Ra}(K_{Th} + \lambda_{Ra})}{F_{Th}(K_{Ra} + \lambda_{Ra})}\left\{1 + \frac{\lambda_{Th}(K_U - K_{Th})}{(K_{Th} + \lambda_{Ra})(K_U + \lambda_{Th})}\right\} \tag{15}$$

where

$$F_i = \frac{\phi\rho_f}{D_i\rho_s(1 - \phi) + \phi\rho_f} \tag{16}$$

and

$$K_i = \frac{F_i(1 - D_i)}{\phi\rho_f}\,\Gamma_o \tag{17}$$

D_i is the bulk mineral/melt partition coefficient and ρ_f and ρ_s are the densities of the melt and peridotite (2800 and 3300 kgm^{-3}). A similar expression to equation 14 can be derived for ($^{231}Pa/^{235}U$).

APPENDIX 2. MAJOR AND TRACE ELEMENT ABUNDANCES OF HAWAIIAN SAMPLES

Table A1. Major- and trace-elements measured by XRF at Los Alamos National Laboratory. Major elements given in weight percent; trace elements given in μg/g. Estimated relative errors on major elements ≈2%, except for Na (5%), P (6%), and K (8%). Estimated relative errors for trace elements are 5–15%. For major- and trace-element compositions of the Loihi samples see Clague et al., 1982; Frey and Clague, 1983.

	Kilauea			Mauna Loa		Mauna Kea	
	Kl-01-KWWS-92	F91-31	F91-32	ML-61-KWWS-92	ML-07-KWWS-92	MK-06-KWWS-92	MK-12-KWWS-92
SiO2	50.01	49.99	49.58	51.37	51.4	50.43	51.65
TiO2	2.45	2.4	2.36	2.09	2.06	2.62	2.32
Al2O3	13.01	12.76	12.80	13.45	13.32	16.76	17.10
FeO(tot)	12.39	12.59	12.48	12.28	12.21	11.48	10.75
MnO	0.17	0.17	0.17	0.17	0.17	0.21	0.22
MgO	7.84	9.04	9.21	7.13	8.53	4.00	3.57
CaO	11.07	10.62	10.68	10.53	10.35	6.64	6.35
Na2O	2.19	2.13	2.05	2.36	2.24	4.82	5.05
K2O	0.45	0.41	0.40	0.38	0.41	2.00	2.11
P2O5	0.23	0.23	0.23	0.22	0.24	0.86	0.95
total	99.81	100.34	99.96	99.98	100.92	99.82	100.07
Ni	100.			67.7	148		
Cr	431.	890	610	263	413		
Y	26.1			27.3	25.5	46.0	49.2
V	287.	271	293	271	274	90.6	37.6
Nb	44			9.82	11.5	51.3	60.1
Zn	102.	<40	<21	79.8	96.3	120.	130.
Ba		<1100	<800	82.8	104	591.	680.
Rb	7.8			6.3	6.5	37.8	34.2
Sr	329.			310.	326	1257.	1241.

	Hualalai				Haleakala				
	HU-05-KWWS-92	HU-10-KWWS-92	HU-18-KWWS-92	HU-24-KWWS-92	HK-02-KWWS-92	HK-04-KWWS-92	HK-06-KWWS-92	HK-10-KWWS-92	HK-11-KWWS-92
SiO2	45.92	46.9	46.23	45.59	44.56	42.46	42.57	42.64	43.05
TiO2	2.32	2.46	2.19	2.38	3.08	2.90	3.61	3.61	3.61
Al2O3	14.29	14.48	14.08	14.08	14.92	11.97	12.55	12.51	12.77
FeO(tot)	13.76	13.74	13.92	14.04	14.18	15.18	14.99	14.99	14.7
MnO	0.18	0.18	0.18	0.18	0.12	0.19	0.19	0.19	0.20
MgO	8.77	7.66	9.63	9.47	7.23	11.89	8.36	8.30	8.30
CaO	10.45	10.4	10.25	9.71	10.19	11.02	12.53	12.57	12.51
Na2O	2.88	2.98	2.87	2.97	3.8	2.68	3.37	3.39	3.43
K2O	0.94	1.02	0.9	0.97	1.37	0.93	1.32	1.3	1.37
P2O5	0.29	0.31	0.27	0.31	0.52	0.33	0.51	0.50	0.50
total	99.8	100.14	100.53	99.70	100.05	99.55	100.00	100.00	100.44
Ni	153	134.	217	194	83.4	260.	112.	109.	121.
Cr	350.	232	409	361	247.	593.	221.	241.	234.
Y	22.8	29.2	21.0	21.7	29	25.7	24.8	25.7	26.1
V	315.	347.	324.	305.	276.	323.	373.	378.	394.
Nb	23.6	27.6	24.9	26.4	41.6	33.1	57.5	47.0	50.2
Zn	82.	95.4	96.2	91.4	66.6	67.1	78.0	49.9	125.
Ba	285.	326	257.	334.	552.	378.	517.	518.	504.
Rb	23.2	24	23	24	33.2	22.9	32.3	30.4	32.6
Sr	480.	457.	449.	494.	772.	531.	787.	792.	778.

Table A2. Trace-elements measured by ICP-MS at the University of Arizona (A); and Washington State University (B). For the REE-Ce, Pr, Nd, Sm, Gd, Dy, Yb, and Lu and Ba, Nb, Y, Rb, Sr and Sc estimated relative errors are ≈5%, for La, Tb, Ho, Er, and Tm, and U and Th estimated relative errors are ≈10%. For samples where the REE have been measured by both laboratories, the LREE values measured at the Washington State University are lower but preferred: 1) there is excellent agreement between the REE concentrations measured for USGS ref. material BHVO-1 at Washington State University (submitted as a blind standard) and (c) the accepted consensus values for this standard (Gladney and Roelandts, 1988); 2) there is also good agreement between the Sm and Nd concentrations measured at Washington State University and those measured at UCB by ID-TIMS (Appendix II-Table 3).

	Kilauea			Mauna Loa	
	Kl-01-KWWS-92 (A)	F91-31 (B)	F91-32 (B)	ML-61-KWWS-92 (A)	ML-07-KWWS-92 (B)
La (ppm)	12.7	12.36	12.25	10.0	10.15
Ce (ppm)	32.4	28.2	28.37	27.3	23.82
Pr (ppm)	4.27	4.20	4.23	3.66	3.6
Nd (ppm)	21.3	19.52	19.67	16.7	16.66
Sm (ppm)	5.31	5.48	5.43	4.79	4.85
Eu (ppm)	1.81	1.81	1.84	1.90	1.61
Gd (ppm)	6.27	5.8	5.92	6.01	5.25
Tb (ppm)	0.93	0.91	0.91	0.94	0.82
Dy (ppm)	5.33	5.02	5.16	5.19	4.64
Ho (ppm)	0.92	0.95	0.95	0.97	0.88
Er (ppm)	2.51	2.41	2.5	2.68	2.37
Tm (ppm)	0.32	0.34	0.35	0.33	0.34
Yb (ppm)	1.98	2.00	2.05	2.24	1.93
Lu (ppm)	0.28	0.30	0.31	0.32	0.29
U (ppm)	**	0.22	0.22	**	0.16
Th (ppm)	**	0.77	0.78	**	0.55
Ba (ppm)	**	105	103	**	93
Nb (ppm)	**	13.21	13.28	**	9.47
Y (ppm)	**	27.97	27.63	**	25.94
Hf (ppm)	**	3.68	3.72	**	3.20
Ta (ppm)	**	0.85	0.87	**	0.60
Rb (ppm)	**	7.62	7.36	**	7.08
Sr (ppm)	**	327	325	**	326
Sc (ppm)	**	33.1	32.6	**	30.3

	Mauna Kea			Hualalai				
	MK-06-KWWS-92 (A)	MK-12-KWWS-92 (B)#1	MK-12-KWWS-92 (B)#2	HU-05-KWWS-92 (A)	HU-05-KWWS-92 (B)	HU-10-KWWS-92 (B)	HU-18-KWWS-92 (B)	HU-24-KWWS-92 (B)
La (ppm)	51.2	59.86	60.91	22.80	19.13	17.65	18.62	20.73
Ce (ppm)	123.	127.02	127.97	53.4	39.12	36.19	38.49	41.91
Pr (ppm)	16.0	17.05	17.11	6.25	5.11	4.80	5.03	5.41
Nd (ppm)	67.3	70.81	71.56	27.3	21.21	19.73	21.08	22.41
Sm (ppm)	13.1	15.46	15.66	6.65	5.08	4.6	4.97	5.33
Eu (ppm)	3.68	4.69	4.71	1.86	1.63	1.48	1.60	1.69
Gd (ppm)	11.6	13.50	13.57	7.07	5.05	4.69	4.87	5.21
Tb (ppm)	1.48	1.87	1.88	0.88	0.76	0.72	0.75	0.79
Dy (ppm)	8.71	9.77	9.79	5.03	4.29	4.1	4.24	4.39
Ho (ppm)	1.49	1.73	1.77	0.88	0.80	0.78	0.81	0.82
Er (ppm)	3.80	4.33	4.48	2.31	2.16	2.08	2.09	2.15
Tm (ppm)	0.51	0.6	0.61	0.29	0.3	0.29	0.30	0.3
Yb (ppm)	3.07	3.45	3.52	1.87	1.8	1.72	1.73	1.78
Lu (ppm)	0.41	0.51	0.52	0.28	0.27	0.26	0.27	0.27
U (ppm)	**	0.96	0.97	**	0.35	0.31	0.33	0.38
Th (ppm)	**	3.84	3.80	**	1.45	1.30	1.42	1.54
Ba (ppm)	**	675	685	**	298	262	290	313
Nb (ppm)	**	64.05	57.48	**	25.18	21.88	23.32	26.64
Y (ppm)	**	50.99	50.54	**	23.59	22.88	22.87	24.54
Hf (ppm)	**	10.90	10.69	**	3.69	3.12	3.37	3.68
Ta (ppm)	**	3.86	3.53	**	1.63	1.38	1.49	1.66
Rb (ppm)	**	35.92	35.56	**	22.75	16.84	22.44	24.46
Sr (ppm)	**	1237	1219	**	475	406	452	506
Sc (ppm)	**	8.2	7.9	**	27.7	33.1	27.1	26.6

Table A2. (Continued)

	Haleakala						
	HK-02-KWWS-92 (A)	HK-02-KWWS-92 (B)	HK-04-KWWS-92 (B)	HK-06-KWWS-92 (B)	HK-10-KWWS-92 (B)#1	HK-10-KWWS-92 (B)#2	HK-11-KWWS-92 (B)
La (ppm)	37.3	36.55	26.36	38.6	38.73	39.33	42.76
Ce (ppm)	83.5	69.49	51.37	90.1	75.39	77.47	80.38
Pr (ppm)	9.80	8.98	6.66	11.0	9.62	9.83	9.93
Nd (ppm)	37.7	36.9	27.63	42.1	40.21	40.42	39.82
Sm (ppm)	7.99	8.17	6.57	9.45	8.83	9.03	8.84
Eu (ppm)	2.08	2.58	2.1	2.91	2.71	2.75	2.76
Gd (ppm)	7.39	7.61	6.32	8.76	7.87	8.10	8.19
Tb (ppm)	1.00	1.07	0.92	1.19	1.08	1.12	1.16
Dy (ppm)	5.40	5.77	4.88	6.08	5.59	5.70	6.27
Ho (ppm)	0.95	1.05	0.88	1.14	0.95	0.97	1.13
Er (ppm)	2.46	2.59	2.18	2.62	2.25	2.34	2.8
Tm (ppm)	0.28	0.36	0.29	0.32	0.29	0.30	0.38
Yb (ppm)	2.01	2.06	1.69	1.83	1.64	1.66	2.22
Lu (ppm)	0.25	0.3	0.24	0.28	0.24	0.24	0.33
U (ppm)	**	0.72	0.50	**	0.77	0.77	0.83
Th (ppm)	**	3.02	2.13	**	3.05	3.09	3.50
Ba (ppm)	**	564	391	**	539	544	672
Nb (ppm)	**	51.77	36.14	**	52.42	52.96	58.86
Y (ppm)	**	30.39	25.65	**	27.25	27.31	32.28
Hf (ppm)	**	5.14	4.18	**	5.69	5.64	5.18
Ta (ppm)	**	3.06	2.20	**	3.23	3.25	3.44
Rb (ppm)	**	33.11	23.41	**	31.96	32.00	36.79
Sr (ppm)	**	750	529	**	793	786	869
Sc (ppm)	**	22.9	29.7	**	28.4	27.7	20.0

	BHVO-1 (B)	BHVO-1 (C)
La (ppm)	16.91	15.8 ± 1.3
Ce (ppm)	38.23	39 ± 4
Pr (ppm)	5.46	5.7 ± 0.4
Nd (ppm)	24.58	25.2 ± 2
Sm (ppm)	6.35	6.2 ± 0.3
Eu (ppm)	2.06	2.06 ± 0.08
Gd (ppm)	6.35	6.4 ± 0.5
Tb (ppm)	0.95	0.96 ± 0.08
Dy (ppm)	5.32	5.20 ± 0.3
Ho (ppm)	0.99	0.99 ± 0.08
Er (ppm)	2.56	2.4 ± 0.2
Tm (ppm)	0.35	0.33 ± 0.04
Yb (ppm)	2.01	2.02 ± 0.20
Lu (ppm)	0.29	0.29 ± 0.03
U (ppm)	0.33	0.42 ± 0.06
Th (ppm)	0.91	1.08 ± 0.15
Ba (ppm)	135	139 ± 14
Nb (ppm)	18.94	19 ± 2
Y (ppm)	28.38	27.6 ± 1.7
Hf (ppm)	4.42	4.38 ± 0.22
Ta (ppm)	1.25	1.23 ± 0.13
Rb (ppm)	9.66	11 ± 2
Sr (ppm)	399	403 ± 25
Sc (ppm)	31.9	31.8 ± 1.3

Table A3. Sm and Nd concentrations and Nd and Sr isotopes measured by TIMS.

Sample	Sm[1] ppm	Nd[1] ppm	$^{147}Sm/^{144}Nd$[2]	ε_{Nd}[3]	$^{87}Sr/^{86}Sr$[4]
Loihi					
KK-19-1 (WR)	4.26	16.72	0.1541	4.9	0.70357
KK-19-1 (Gl)	4.29	16.84	0.1541	5.0	0.70355
KK-27-14	3.65	15.71	0.1405	5.5	0.70347
Kilauea					
KL-01-KWWS-92	5.33	19.87	0.1622	6.1	0.70359
KL-F91-31	4.38	16.45	0.1611	6.4	0.70355
KL-F91-32					
Mauna Loa					
ML-61-KWWS-92	4.79	16.67	0.1737	4.4	0.70380
ML-07-KWWS-92	4.67	16.77	0.1682	5.1	0.70360
Mauna Kea					
MK-06-KWWS-92	14.16	66.18	0.1294	7.1	0.70345
MK-12-KWWS-92					
Hualalai					
HU-05-KWWS-92	5.04	22.13	0.1379	5.2	0.70360
HU-10-KWWS-92					
HU-18-KWWS-92					
HU-24-KWWS-92	5.12	22.78	0.1359	5.7	0.70357
Haleakala					
HK-02-KWWS-92	8.08	37.84	0.1291	7.7	0.70325
HK-04-KWWS-92	6.67	29.08	0.1387	7.5	0.70327
HK-06-KWWS-92	8.72	40.53	0.1301	8.3	0.70310
HK-10-KWWS-92	9.15	41.82	0.1324	7.9	0.70311
HK-11-KWWS-92	10.57	49.01	0.1305	8.2	0.70310

[1] Concentrations measured by ID-TIMS; measurement errors $\leq$0.4%.
[2] Measurement errors (2σ) range from 0.1%–0.2%.
[3] $^{143}Nd/^{144}Nd$ ratios, expressed in terms of ε_{Nd} (see DePaolo, 1988), normalized to $^{146}Nd/^{142}Nd = 0.636151$ and are relative to 0.511831 ± 17 for BCR-1 (our measured values at BCIG); measurement errors, based on in-run statistics, (2σ) ≤ 0.30 ε_{Nd} units.
[4] Measurement errors, based on in-run statistics, (2σ) ≤ 0.00002 and are relative to 0.710250 ± 14 for NBS-987.